The Impact of the African Great Lakes on the Regional Climate

Wim Thiery

Department of Earth and Environmental Sciences, KU Leuven, Leuven, Belgium

Edouard L. Davin

Institute for Atmospheric and Climate Science, ETH Zürich, Zürich, Switzerland

Hans-Jürgen Panitz

Institute for Meteorology and Climate Research, Karlsruhe Institute of Technology, Karlsruhe, Germany

Matthias Demuzere, Stef Lhermitte, and Nicole van Lipzig

Department of Earth and Environmental Sciences, KU Leuven, Leuven, Belgium

(Manuscript received 21 July 2014, in final form 2 February 2015)

ABSTRACT

Although the African Great Lakes are important regulators for the East African climate, their influence on atmospheric dynamics and the regional hydrological cycle remains poorly understood. This study aims to assess this impact by comparing a regional climate model simulation that resolves individual lakes and explicitly computes lake temperatures to a simulation without lakes. The Consortium for Small-Scale Modelling model in climate mode (COSMO-CLM) coupled to the Freshwater Lake model (FLake) and Community Land Model (CLM) is used to dynamically downscale a simulation from the African Coordinated Regional Downscaling Experiment (CORDEX-Africa) to 7-km grid spacing for the period of 1999–2008. Evaluation of the model reveals good performance compared to both in situ and satellite observations, especially for spatiotemporal variability of lake surface temperatures (0.68-K bias), and precipitation (-116 mm yr^{-1} or 8% bias). Model integrations indicate that the four major African Great Lakes almost double the annual precipitation amounts over their surface but hardly exert any influence on precipitation beyond their shores. Except for Lake Kivu, the largest lakes also cool the annual near-surface air by -0.6 to -0.9 K on average, this time with pronounced downwind influence. The lake-induced cooling happens during daytime, when the lakes absorb incoming solar radiation and inhibit upward turbulent heat transport. At night, when this heat is released, the lakes warm the near-surface air. Furthermore, Lake Victoria has a profound influence on atmospheric dynamics and stability, as it induces circular airflow with over-lake convective inhibition during daytime and the reversed pattern at night. Overall, this study shows the added value of resolving individual lakes and realistically representing lake surface temperatures for climate studies in this region.

1. Introduction

The African Great Lakes (AGL) represent the largest reservoir of freshwater lakes in the tropics, including the second largest freshwater lake on earth in terms of surface area (Lake Victoria, 68 800 km^2) and the second largest in terms of volumetric water storage (Lake Tanganyika, 17 800 km^3). The AGL provide numerous ecosystem services to local communities, such as fishing resources, drinking water, and electrical power. Lake Victoria alone directly supports 200 000 fishermen operating from its shores and sustains the livelihood of more than 30 million people living at its coasts (Semazzi 2011).

Lakes also influence regional climate conditions, in particular in regions where they are abundant. Mediated by the fluxes of energy, moisture, and momentum, they significantly alter the surface energy and water balance in a particular region and therefore its climate. Such reciprocal relations are often studied using numerical

Corresponding author address: Wim Thiery, Department of Earth and Environmental Sciences, KU Leuven, Celestijnenlaan 200E, 3001 Leuven, Belgium.
E-mail: wim.thiery@ees.kuleuven.be

models. At the global scale, general circulation model (GCM) studies demonstrate an average annual cooling effect of lakes but also highlight important seasonal and regional effects (Bonan 1995; Subin et al. 2012; Rooney and Bornemann 2013). Numerous studies also mention the increase in annual precipitation due to the presence of lakes (e.g., Coe and Bonan 1997). Regional climate model (RCM) studies have been performed at higher horizontal resolution (e.g., 50 km), thereby better emphasizing the lake–atmosphere interplay at the local scale (e.g., Hostetler et al. 1994; Hostetler and Giorgi 1995; Bates et al. 1995; Goyette et al. 2000; Anyah et al. 2006; Samuelsson et al. 2010; Gula and Peltier 2012; Lauwaet et al. 2012; Martynov et al. 2012; Gu et al. 2015; Notaro et al. 2013; Bennington et al. 2014; Williams et al. 2015).

Although the AGL are widely recognized as an important driver of the East African regional climate system, their impact on atmospheric dynamics and the regional hydrological cycle remains poorly understood. Studies on the interplay between climate and the AGL are therefore necessary to identify, among other information, the patterns of evaporation and precipitation induced by lake presence and the reasons behind their observed spatiotemporal variability. The need to enhance the understanding is urgent, as every year, possibly more than 5000 fishermen lose their lives over Lake Victoria alone, mostly due to hazardous weather conditions and associated water currents (Semazzi 2011).

The poor understanding of African lake–climate interactions is related to a number of challenges when applying a regional climate model to the AGL region: (i) First, a model should be applicable to tropical conditions. Among other requirements, such a setup must be able to reproduce tropical features, such as deep convection or mesoscale convective systems [and associated precipitation extremes; Lauwaet et al. (2009); Goyens et al. (2012)] and must include a land surface model (LSM) capable of simulating tropical vegetation. In recent climate model studies over tropical Africa, these challenges have received particular attention (e.g., Vizy and Cook 2012; Saeed et al. 2013; Crétat et al. 2014; Panitz et al. 2014; Dosio et al. 2015). (ii) Second, the horizontal model grid resolution should be sufficiently high to resolve individual lakes and strong orography of the region. Combined with the long integration period and high vertical extent necessary to model tropical climatic conditions, the need for computational resources rises. (iii) Third, a correct representation of lake surface temperatures within the atmospheric model is essential to investigate the two-way interactions between climate and lake processes over East Africa (Stepanenko et al. 2013). This can be particularly

challenging for large, deep lakes given the role of vertical heat transport and three-dimensional water circulation within these lakes (Gu et al. 2015; Bennington et al. 2014). (iv) Last, the limited number of observational datasets available and issues regarding the quality of available products over highly mountainous, tropical domains (e.g., Dinku et al. 2008) complicate a comprehensive model evaluation over this region. Consequently, up to now only a few RCM studies explicitly examine aspects of lake–atmosphere interactions over a specific African Great Lake (Savijärvi and Järvenoja 2000; Song et al. 2004; Anyah and Semazzi 2004; Anyah et al. 2006; Argent et al. 2015; Sun et al. 2014a,b; Williams et al. 2015), while none investigates these interactions for the whole region.

Hence, the main goals of this study are to assess the regional climate impact of the AGL and understand the physical mechanisms underlying these impacts. This is achieved by addressing the aforementioned challenges in the following ways: (i) The regional Consortium for Small-Scale Modelling model in climate mode (COSMO-CLM; Rockel et al. 2008) is applied in its tropical setup [configuration following Panitz et al. (2014)]. In their comprehensive evaluation of the COSMO-CLM evaluation simulation conducted in the framework of the African Coordinated Regional Downscaling Experiment (CORDEX-Africa; Giorgi et al. 2009), Panitz et al. (2014) demonstrate the ability of COSMO-CLM to reproduce the overall features of the African climate (when downscaling ERA-Interim) and show that, relative to several gridded observational products, it even outperforms ERA-Interim in terms of the mean annual precipitation cycles and interannual variability over major parts of the domain. Among the considered regional biases, the authors point to an underestimation of the precipitation intensity by $2\,\mathrm{mm\,day^{-1}}$ in East Africa, which is ascribed to an underestimation of the latent heat flux and overestimation of the sensible heat flux. To address this issue, here we employ COSMO-CLM coupled to a state-of-the-art LSM, the Community Land Model, version 3.5 (CLM3.5; Davin and Seneviratne 2012). For various applications, this version already showed improved skills compared to the standard version (see section 2a). (ii) Model integrations are performed for a period of 13 years on a horizontal resolution high enough for large to medium-sized lakes to become resolved features (0.0625°; ~7 km). (iii) The one-dimensional Freshwater Lake model (FLake), recently coupled to COSMO-CLM (Mironov et al. 2010), is used to compute lake water surface temperatures. (iv) Special attention is paid to model evaluation, in particular by using remote sensing products and comprehensive in situ observational datasets to assess the model's ability to reproduce

observed spatial and temporal lake surface temperature variability, turbulent fluxes, and precipitation. Adopting one or more of the above challenges may improve the representation of the regional climate, as demonstrated in many recent studies (e.g., Mironov et al. 2010; Nikulin et al. 2012; Akkermans 2013; Laprise et al. 2013; Akkermans et al. 2014; Crétat et al. 2014; Dosio et al. 2015; Williams et al. 2015).

Within this paper, the results of the RCM control simulation are extensively evaluated. This simulation is subsequently compared to a no-lake simulation, where the lakes are replaced by representative land pixels. This approach makes it possible to quantify the impact on the regional climate, in particular on near-surface temperature and precipitation. The impact of the lakes is then investigated in more detail by applying a surface energy balance decomposition technique and studying the dynamical changes induced by the lakes.

2. Model, data, and methodology

a. COSMO-CLM²

To investigate the influence of the AGL on the climate, we use the three-dimensional, nonhydrostatic regional climate model, COSMO-CLM (Rockel et al. 2008), version 4.8. The model development is a joint effort of the Consortium for Small-Scale Modelling and the Climate Limited-Area Modelling Community (CLM-Community). Its dynamical core solves the fully compressible hydrothermodynamical equations for three-dimensional Cartesian wind components; pressure perturbation; temperature; specific humidity; cloud water content and optionally cloud ice content; turbulent kinetic energy; and rain, snow, and graupel specific water content (Doms 2011). Physical parameterizations include a description of subgrid-scale turbulence (Raschendorfer 2001), grid-scale clouds and precipitation (Doms et al. 2011), shallow and moist convection (Tiedtke 1989), and δ-two-stream radiative transfer (Ritter and Geleyn 1992). A detailed description of the model system dynamics, numeric, and physical parameterizations can be found in the model documentation (e.g., Doms 2011; Doms et al. 2011; http://www.cosmo-model.org).

Additionally, the native COSMO-CLM Multi-Layered land surface model (TERRA-ML; Grasselt et al. 2008) is replaced by the more comprehensive Community Land Model (CLM; Oleson et al. 2004, 2008), version 3.5. CLM3.5 is maintained at the National Center for Atmospheric Research (NCAR), and given its explicit treatment of the photosynthetic process and its control on the stomatal conductance (big-leaf approach), it can be considered a third-generation LSM (Sellers et al. 1997).

Moreover, an individual land pixel can be composed of multiple land units due to the nested tile approach, which allows representation of multiple soil columns and represents biomes as a combination of different plant functional types. An extensive description and evaluation of CLM3.5 in offline mode is presented in Oleson et al. (2004, 2008) and Stöckli et al. (2008).

The model system COSMO-CLM coupled to CLM3.5 (hereinafter referred to as COSMO-CLM²) is described in detail by Davin and Seneviratne (2012) and references therein. The added value of COSMO-CLM², relative to the standard setup, was recently demonstrated over Europe (Davin et al. 2011; Davin and Seneviratne 2012; Lorenz et al. 2012) and central Africa (Akkermans 2013). A better partitioning of the turbulent fluxes and associated improvement of climate characteristics, such as near-surface temperature, precipitation, and cloud cover, were found in all cases, supporting the usage of this model for studying biogeophysical impacts of altered land surface characteristics (e.g., Davin et al. 2014; Lejeune et al. 2015; Jacobs et al. 2015; Vanden Broucke et al. 2015). Based on an offline comparison of both LSMs at four central African flux tower sites, Akkermans et al. (2012) attributed this enhanced skill mainly to a more realistic representation of the leaf area index, surface albedo, and root depth in CLM3.5 compared to TERRA-ML. Furthermore, Akkermans et al. (2014) extensively evaluated COSMO-CLM² over the larger central African domain and found a close correspondence between the observed and modeled near-surface temperature, column precipitable water, and surface net longwave radiation. For precipitation, cloud cover, top of the atmosphere outgoing longwave radiation, and various solar radiation quantities, the model adequately reproduced observed values, with some notable differences potentially ascribed to an underestimation of the optical thickness of convective clouds by COSMO-CLM².

b. FLake

As a one-dimensional lake model embedded in COSMO-CLM², FLake computes the evolution of a lake column temperature profile and the integral energy budgets of its different layers (Mironov et al. 2010). The model considers two layers in the water column: a mixed layer at the top and a thermocline down to the lake bottom. While the mixed layer is assumed to have a uniform temperature (T_{ML}), the temperature-depth curve in the thermocline is parameterized through the concept of self-similarity or assumed shape (Kitaigorodskii and Miropolskii 1970). This shape is only dependent on the temperature at its extremities and a shape factor, which describes the curve through a fourth-order polynomial (Mironov 2008). In the absence of snow and ice cover and

when neglecting bottom sediments, the prognostic variables are the mixed layer depth (h_{ML}), the bottom and water column average temperatures (T_{BOT} and T_{MW}, respectively), and the shape factor with respect to the temperature profile in the thermocline (C_T). Given their control on turbulence in the surface mixed layer (Read et al. 2012), h_{ML} is predicted taking convective and mechanical mixing into account, whereas volumetric heating is computed from the net shortwave radiation penetration through the lake surface and absorption at depth according to the Beer–Lambert law. To this end, the default downward light attenuation coefficient of $3 \, m^{-1}$ is employed. A recent global bathymetry dataset (Kourzeneva 2010; Kourzeneva et al. 2012) is used to specify lake depth of each lake pixel, thereby assuming a maximum lake depth of 50 m. A detailed description of FLake is provided in Mironov (2008) and Mironov et al. (2010).

Although FLake is a relatively simple model, its skill proves comparable to other, more comprehensive one-dimensional lake models for various lake types and climatic conditions (e.g., Perroud and Goyette 2009; Stepanenko et al. 2010, 2013, 2014). Moreover, FLake was extensively tested in offline mode over several AGL and judged an adequate tool to compute lake surface temperatures in comparison to other one-dimensional lake models, even though lake bottom temperatures may be sensitive to changes in certain external parameters and driving variables, such as wind speed (Thiery et al. 2014a,b). This is the first study to consider lake–atmosphere interactions over the AGL using FLake interactively coupled to an RCM. Previous RCM studies focusing on Lake Victoria either used prescribed lake surface temperatures (e.g., Anyah and Semazzi 2004; Argent et al. 2015; Sun et al. 2014a; Williams et al. 2015), the Hostetler lake model (e.g., Song et al. 2004), or the Princeton Ocean Model (POM; e.g., Song et al. 2004; Anyah and Semazzi 2006; Sun et al. 2014b).

c. Model setup

To obtain information on small-scale variability, RCMs dynamically downscale lateral boundary conditions at a coarser resolution to a regional finer-scale model grid (Laprise et al. 2008). Here, we use the COSMO-CLM CORDEX-Africa evaluation simulation (Panitz et al. 2014) as lateral boundary conditions. The CORDEX-Africa evaluation simulation represents a dynamical downscaling to a 50-km (0.44°) horizontal grid spacing of the ERA-Interim, made available by the European Center for Medium-Range Weather Forecast (ECMWF; Dee et al. 2011) for 1979–2014 at 79-km (T255) resolution. Given the large difference in resolution between the latter and the target configuration, a direct downscaling of ERA-Interim is not advisable in this case.

The COSMO-CLM^2 model system is used to generate two climate simulations. First, a control simulation (CTL) is conducted where the lakes are included in the model integration. For this purpose, FLake is employed to compute the water temperatures for the AGL. The second simulation [the no-lake simulation (NOL)] is identical to the control experiment, but each lake pixel is replaced by a representative land pixel selected from all land pixels within a distance of 50 km. The external parameters and initial conditions of replaced land pixels consequently show similar values and spatial patterns as the surrounding land; for instance, the area change of various plant functional types (PFTs) within the domain is 0.35% on average and less than 3% for each individual PFT.

Both experiments are conducted at a horizontal resolution of 0.0625° (~7 km), which is finer than previous multiyear RCM experiments over this region (e.g., Sun et al. 1999; Song et al. 2004; Anyah and Semazzi 2004; Anyah et al. 2006; Williams et al. 2015; with resolutions ranging from 20 to 60 km), using 50 vertical levels and a time step of 60 s. The model domain encompasses the central part of the East African rift (Fig. 1) and, therewith, includes most of the AGL. Since enlarging the model domain by 50 grid points (3.125°) in each direction reduced the predictive skill of a 1-yr test simulation and more than doubled the total computation time, this option was not considered. The simulations cover the period 1996–2008 (13 yr), of which the first three years are considered as spin-up time and excluded from the analysis. Inspection of predicted lake water surface temperatures shows that three years is enough to spin up the model: lake water surface temperatures evolve to normal climatological values within the first year already. Finally, on each side, 10 grid points were excluded from the analysis. Computation of the Davies relaxation function (Davies 1983) in the east–west direction showed that direct influence of lateral boundary conditions vanishes beyond this zone. The presence of two north–south oriented mountain ranges within the model domain are expected to further reduce the imprint of the parent model on the COSMO-CLM^2 predictions.

The configuration used in this study is based on the tropical setup of COSMO-CLM described by Panitz et al. (2014) and used for the CORDEX-Africa simulations (Panitz et al. 2014; Dosio et al. 2015). In the tropical configuration, the model top is set to 30 km, and the lower height of the damping layer is increased from 11 to 18 km. In addition, we introduced the following modifications: (i) First, CLM3.5 replaces the default LSM in COSMO-CLM. (ii) Second, FLake is used instead of the Hostetler-based lake model embedded within CLM3.5 (Bonan et al. 2002), as the latter
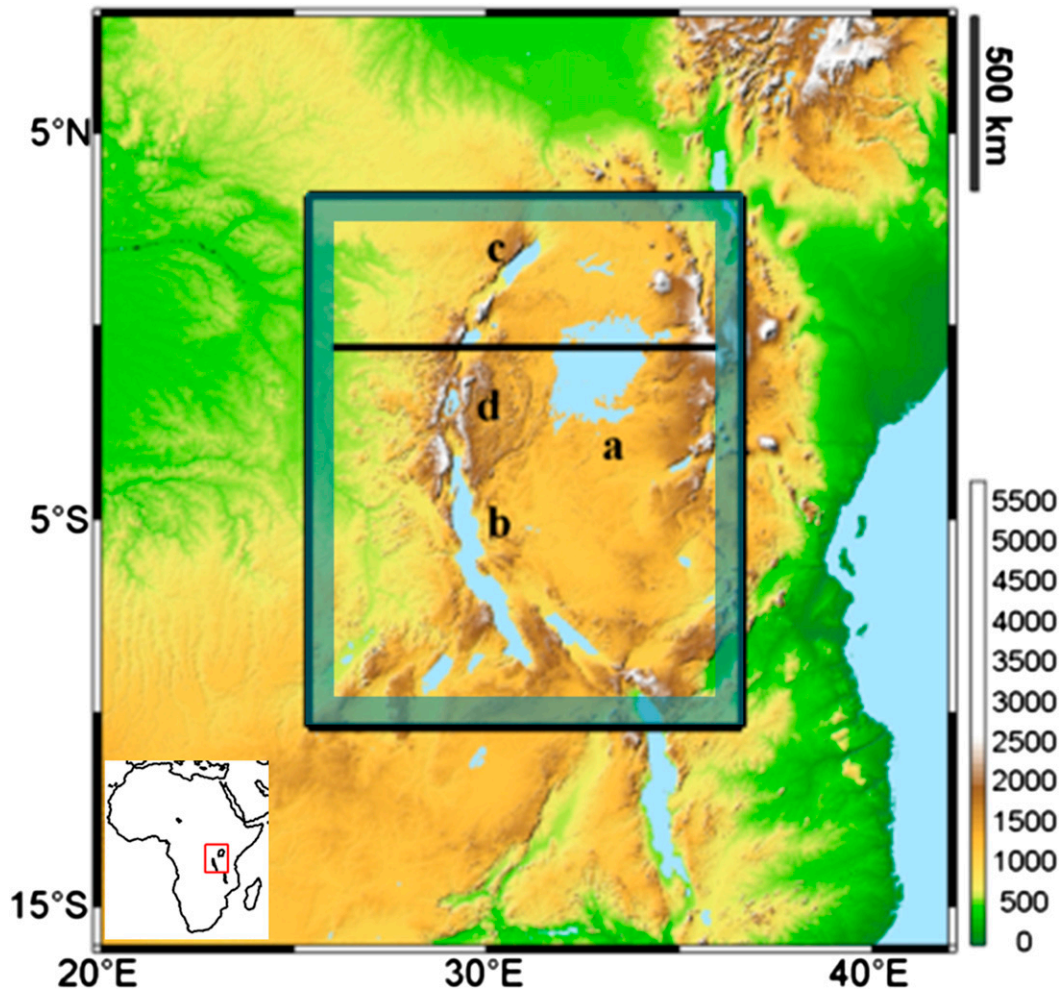
FIG. 1. Shuttle Radar Topography Mission (SRTM) surface height (m) over the African Great Lakes region. The model domain used in this study is denoted by the black rectangle (10.375°S–3.375°N, 25.375°–36.625°E; center at 3.5°S, 31°E) and a 10-gridpoint-wide zone excluded from the analysis by the blue band. The transect (26°–36°E, 0.55°S) used for the vertical cross section in Figs. 13 and 14 is shown by the black line. The four largest African Great Lakes within the model domain are (a) Lake Victoria, (b) Lake Tanganyika, (c) Lake Albert, and (d) Lake Kivu.

exhibits a cold lake temperature bias over the AGL (Thiery et al. 2014b). As recommended by Thiery et al. (2014a), the lake temperature profile is initialized with stratified conditions, an approach also adopted by Hernández-Díaz et al. (2013). (iii) Last, certain model settings (e.g., time step, number of vertical layers, and width of the relaxation layer) were adapted to be consistent with the higher horizontal grid resolution.

d. Evaluation datasets

The performance of the CTL simulation is assessed by comparing model output to observational products for various quantities (see Table 1 for their technical specifications). For precipitation, we use gridded datasets from the following sources: the Global Precipitation

Climatology Project (GPCP; Huffman et al. 2001), the Global Precipitation Climatology Centre (GPCC; Rudolf et al. 2011), the University of Delaware (UDEL; Legates and Willmott 1990), the Climate Prediction Center Morphing Technique (CMORPH; Joyce et al. 2004), and satellite-derived precipitation rates from the Tropical Rainfall Measurement Mission (TRMM) products 3B42 and 2B31 (Kummerow et al. 2000). The TRMM 2B31 product is a combined rainfall-profile product derived from the Precipitation Radar and TRMM Microwave Imager (Bookhagen and Strecker 2008). Since the standard TRMM precipitation product (3B42) and CMORPH demonstrate poor performance over complex African terrain (Dinku et al. 2008), the TRMM 2B31 product is preferred over 3B42, given the

TABLE 1. Data products used for model evaluation (SRes.: spatial resolution; TRes.: temporal resolution).

Variable, symbol (units)	Dataset	Version	Source	SRes.	TRes.	Years	References
Precipitation, P (mm month^{-1})	TRMM	3B42	Mixed	0.25°	Monthly	1999–2008	Kummerow et al. (2000)
—	TRMM	2B31	Satellite	~0.04°	~1.5-hourly	1999–2008	Kummerow et al. (2000)
—	GPCP	1DD	Mixed	1.00°	Daily	1999–2008	Huffman et al. (2001)
—	GPCC	v6	Stations	0.50°	Monthly	1999–2008	Rudolf et al. (2011); Schneider et al. (2014)
—	UDEL	v3.01	Stations	0.50°	Monthly	1999–2008	Legates and Willmott (1990)
—	CMORPH	ds502.0	Mixed	0.25°	3-hourly	2003–08	Joyce et al. (2004); Climate Prediction Center (2011)
Near-surface temperature, T_{2m} (K)	in situ	—	Stations	—	Daily	1999–2008	Nyeko-Ogiramoi et al. (2010, 2013)
Lake surface temperature, T_S (K)	in situ	—	Stations	—	Daily	1999–2008	Plisnier et al. (2000)
	ARC-Lake	v1.1.2	Satellite	0.05°	Variable	1999–2008	MacCallum and Merchant (2012)
Lake water temperature, $T_{0.5m}$ (°C)	in situ	—	Stations	—	Bimonthly	1999–2008	Plisnier et al. (2009); Darchambeau et al. (2014)
Surface net shortwave radiation, SW$_{net}$ (W m^{-2})	GEWEX-SRB	REL3.0	Satellite	1.0°	Monthly	1999–2007	Stackhouse et al. (2011)
Surface net longwave radiation, LW$_{net}$ (W m^{-2})	GEWEX-SRB	REL3.1	Satellite	1.0°	Monthly	1999–2007	Stackhouse et al. (2011)
Latent heat flux, LHF (W m^{-2})	LandFlux-EVAL	—	Mixed	1.0°	Monthly	1999–2005	Mueller et al. (2013)
Sensible heat flux, SHF (W m^{-2})	FLUXNET-MTE	—	Stations	0.50°	Monthly	1999–2008	Jung et al. (2010)
Cloud cover fraction, CCF (%)	ISCCP	D2	Satellite	2.5°	Monthly	1999–2008	Rossow and Schiffer (1999)

higher spatial resolution and ability to reproduce orographically induced precipitation patterns over complex terrain (Bookhagen and Burbank 2006; Bookhagen and Strecker 2008; Burbank et al. 2012). The high-spatial-resolution TRMM 2B31 1999–2008 data were reprojected from their original 4.3–5-km resolution to the 0.0625° grid using a bilinear interpolation algorithm to account for projection and resolution inhomogeneities (Bookhagen and Strecker 2008). The precipitation rates (mm h^{-1}) from each satellite overpass ($\sim$16 day^{-1}) were subsequently rescaled to monthly mean precipitation values using the number of measurements within each grid cell, after which a convolution filter with a 5×5 equal weights window was applied. Note that no further calibration of the data was performed. Finally, a dataset of in situ daily accumulated precipitation measurements was compiled. A similar approach was followed for observed monthly and daily mean near-surface temperature observations; however, measurements of this type are very sparse in the region.

Particular attention is paid to the model's ability to reproduce observed lake surface water temperatures (LSWT), using both in situ and satellite measurements as a reference. To this end, the Along-Track Scanning Radiometers (ATSR) Reprocessing for Climate: LSWT and ice cover (ARC-Lake) project provides high-resolution, spatially explicit global LSWT observations (MacCallum and Merchant 2012). The lake temperature evaluation is complemented using 419 conductivity–temperature–depth (CTD) casts collected during daytime at three multiyear monitoring sites: Ishungu (Lake Kivu), Kigoma (Lake Tanganyika's northern basin) and Mpulungu (Lake Tanganyika's southern basin) (Plisnier et al. 2009; Darchambeau et al. 2014). Vertical piecewise cubic Hermite interpolation (increment 0.1 m; De Boor 1978) was applied to each cast, after which the near-surface water temperature (0.5 m) was extracted and used as a reference. This depth is assumed to be the depth closest to the surface with a reliable measurement from the CTD cast.

The net surface shortwave (SW$_{net}$) and longwave (LW$_{net}$) radiation, latent heat flux (LHF), and sensible heat flux (SHF) were compared to satellite-derived values available from the Global Energy and Water Cycle Experiment Surface Radiation Budget (GEWEX-SRB; Stackhouse et al. 2011), the benchmark synthesis of available diagnostic evapotranspiration estimates (LandFlux-EVAL; Mueller et al. 2013), and the global upscaling of observations from eddy-covariance flux towers using the Flux Network Multi-Tree Ensembles (FLUXNET-MTE; Jung et al. 2010), respectively. The MTE approach represents a machine learning algorithm integrating in situ flux measurements with satellite

observations and surface meteorological data to produce global gridded evapotranspiration estimates and associated uncertainties (Jung et al. 2009). Finally, the cloud cover fraction (CCF) is evaluated using the International Satellite Cloud Climatology Project (ISCCP) D2 dataset (Rossow and Schiffer 1999).

All gridded datasets used are available for the entire analysis period, except for CMORPH (2003–08), LandFlux-EVAL (1999–2005), and GEWEX-SRB (1999–2007). Aside from ARC-Lake, their horizontal resolution is usually much coarser than the CTL simulation (Table 1). No height correction, gap filling, or other modifications were applied to the various datasets. The COSMO-CLM^2 rotated model grid is considered as the reference grid to which all other gridded products are remapped using bilinear interpolation. Evaluation with in situ data is performed by comparing the observed time series to the model grid box encompassing the measurement site.

e. Surface energy balance decomposition

The energy balance at the surface–atmosphere interface is given by

$$\epsilon\sigma T_s^4 = (1 - \alpha)\text{SW}_{\text{in}} + \text{LW}_{\text{in}} - \text{LHF} - \text{SHF} - G, \quad (1)$$

where ϵ is the surface emissivity, σ is the Stefan–Boltzmann constant ($5.67 \times 10^{-8}\,\text{W}\,\text{m}^{-2}\,\text{K}^{-4}$), T_s is the surface temperature, α is the surface albedo with respect to shortwave radiation, SW_{in} is the incoming shortwave radiation, LW_{in} is the incoming longwave radiation, LHF and SHF are the turbulent fluxes of latent heat and sensible heat, and G is the combined subsurface storage and conductive heat fluxes.

The causes for the surface temperature response to the presence of lakes are investigated using a surface energy balance decomposition method developed by Juang et al. (2007) and further modified by Luyssaert et al. (2014) and Akkermans et al. (2014). The net impact of the AGL on surface temperature is decomposed a posteriori and attributed to direct contributions of modified biogeophysical processes (such as surface reflection and evapotranspiration) and indirect contributions due to atmospheric feedbacks (such as cloud radiative feedbacks or surface layer stability changes).

The net change in outgoing longwave radiation is given by $4\epsilon\sigma T_s^3\delta T_s$: that is, the first-order derivative of the left hand side in Eq. (1) with respect to T_s. Note that here, the term surface temperature (T_s) denotes the surface radiative temperature at which the soil–vegetation–lake complex emits longwave radiation to the atmosphere. From this, δT_s can be derived by solving the total derivative of the Eq. (1) and solving for δT_s:

$$\delta T_s = \frac{1}{4\epsilon\sigma T_s^3}[-\text{SW}_{\text{in}}\delta\alpha + (1 - \alpha)\delta\text{SW}_{\text{in}} + \delta\text{LW}_{\text{in}}$$
$$- \delta\text{LHF} + \delta\text{SHF} - \delta G - \sigma T_s^4\delta\epsilon], \quad (2)$$

with δSHF encompassing the SHF changes induced by the modified aerodynamic resistance and the modified temperature gradient. Most terms in Eq. (2) can be calculated from the difference between mean quantities in the control and no-lake simulation (CTL minus NOL), except for $\delta\epsilon$, which is recomputed from the model equations.

3. Results

a. Model evaluation

1) PRECIPITATION AND AIR TEMPERATURE

Observed precipitation patterns are reasonably reproduced by COSMO-CLM^2, in terms of spatial patterns (Fig. 2) as well as the amplitude and phase of the annual cycle (Fig. 3). The model captures the enhanced precipitation in the northwestern part of the domain, associated with strong orographically induced convection in a region where tropical rainforest is the dominant land cover type (Figs. 2a–g). However, the disagreement between the various observational products regarding the magnitude of precipitation over this part of the domain is large (with differences locally exceeding 3900 mm yr^{-1}; Fig. 2h), and the bias is either positive or negative, depending on the benchmark product considered. Generally, the limited number of rain gauges within the model domain and the numerous data gaps in the available time series call for cautious use of gridded precipitation datasets based on in situ measurements, but also satellite-based or mixed-source products contain important uncertainties over the mountainous regions of tropical Africa (e.g., Dinku et al. 2008; Nikulin et al. 2012; Endris et al. 2013; Sylla et al. 2013). Furthermore, COSMO-CLM^2 is able to reproduce the higher precipitation observed by TRMM 3B42 and TRMM 2B31 over some AGL, especially during the wet seasons [March–May (MAM) and October–December (OND), see below]. In particular, the strong precipitation signal over Lake Kivu is reproduced, while the spatial pattern of precipitation over Lake Victoria is reproduced but underestimated relative to both TRMM products. The dry bias over Lake Victoria relative to TRMM 3B42 and 2B31 amounts to −493 mm yr^{-1} (−24%) and −691 mm yr^{-1} (−30%), respectively, and is centered over the western half of the lake, as the modeled precipitation maximum is shifted towards the northeast. Relative to GPCP and CMORPH, in contrast, COSMO-CLM^2 overestimates precipitation over Lake Victoria by 217 mm yr^{-1} (16%) and 250 mm yr^{-1}
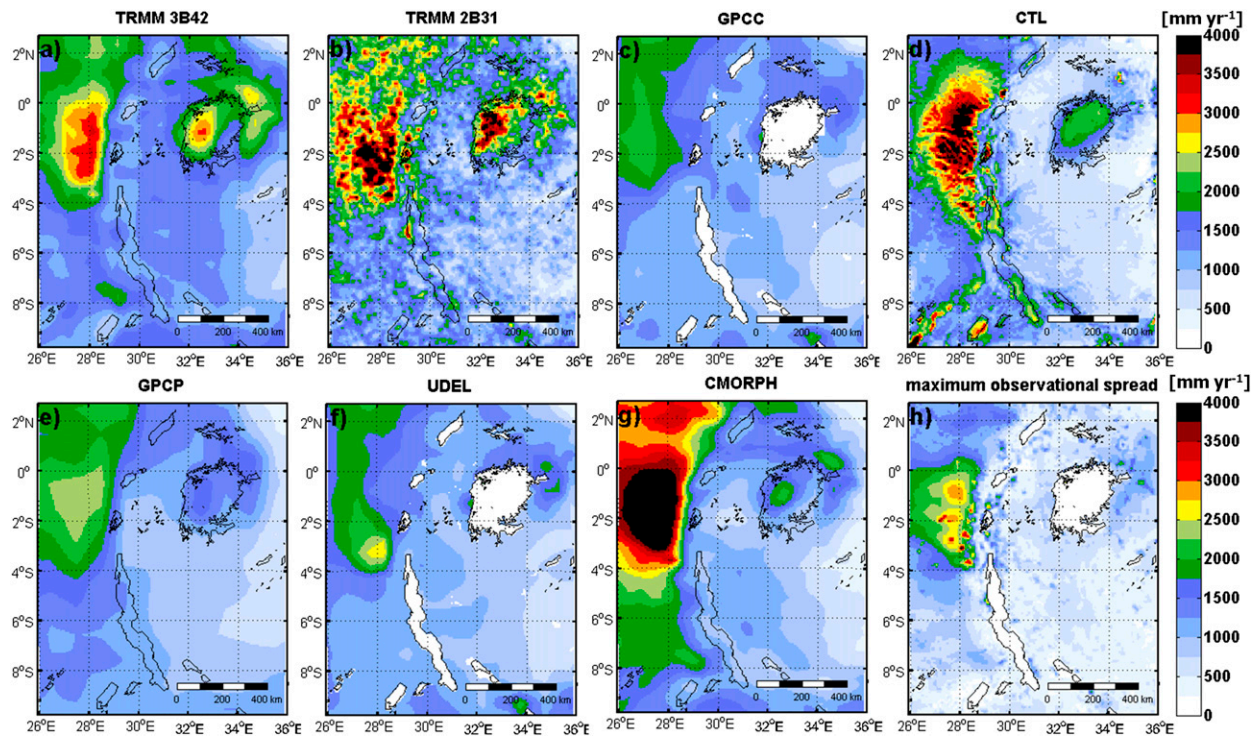
FIG. 2. Observed annual mean precipitation P (mm yr^{-1}) from the datasets described in Table 1—(a) TRMM 3B42, (b) TRMM 2B31, (c) GPCC, (e) GPCP, (f) UDEL, and (g) CMORPH—averaged over the period 1999–2008 (CMORPH data is averaged over 2003–08). (d) The 1999–2008 modeled P (CTL). (h) Maximum difference among observational products, considering only land pixels. The observational products GPCC and UDEL are masked out over the lakes, as they are based solely on land station data.

(19%), respectively. Again, the maximum difference between the gridded observational products is large (1131 mm yr^{-1} averaged over Lake Victoria; Fig. 2h), and largely exceeds the biases between COSMO-CLM^2 and individual products. Such a large spread calls for further research to quantify the uncertainties of observed precipitation in the region. Furthermore, over the central plateau, where the observational products agree fairly well, a dry bias is apparent. This is confirmed by the comparison to in situ precipitation records, located mostly on the central plateau (Figs. 4a,b). Over 75% of the domain, the absolute precipitation bias against individual products remains below 185 mm yr^{-1}, corresponding to 13% of the average precipitation observed over the region (observational ensemble mean).

Seasonal precipitation variability in the AGL region is primarily governed by the north–south migration of the intertropical convergence zone (ITCZ) across the region (Nicholson 1996; Williams et al. 2015). Monthly mean precipitation subsequently indicates a bimodal distribution with a distinct dry season during June–August (JJA) and two wet seasons: MAM (long rains; northward ITCZ migration) and OND (short rains; southward ITCZ migration), separated by the slight

decrease in rainfall during January–February (JF) (little dry season; Fig. 3). The annual cycle of precipitation is reasonably captured by COSMO-CLM^2; averaged over the entire domain, fair correspondence exists between
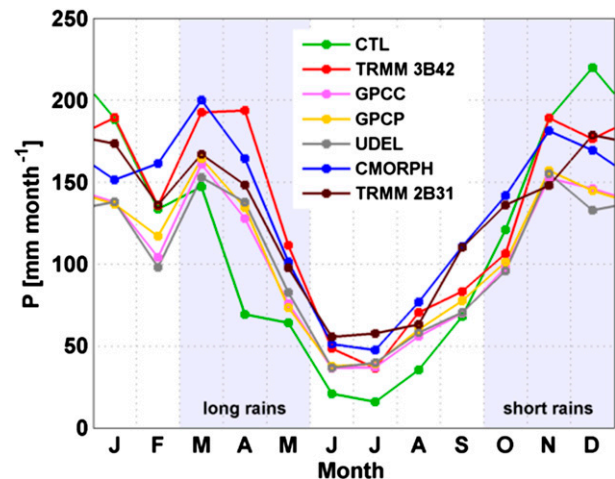

FIG. 3. Observed and modeled domain-averaged seasonal precipitation cycles (mm month^{-1}) over the period 1999–2008 (CMORPH data is averaged over 2003–08).
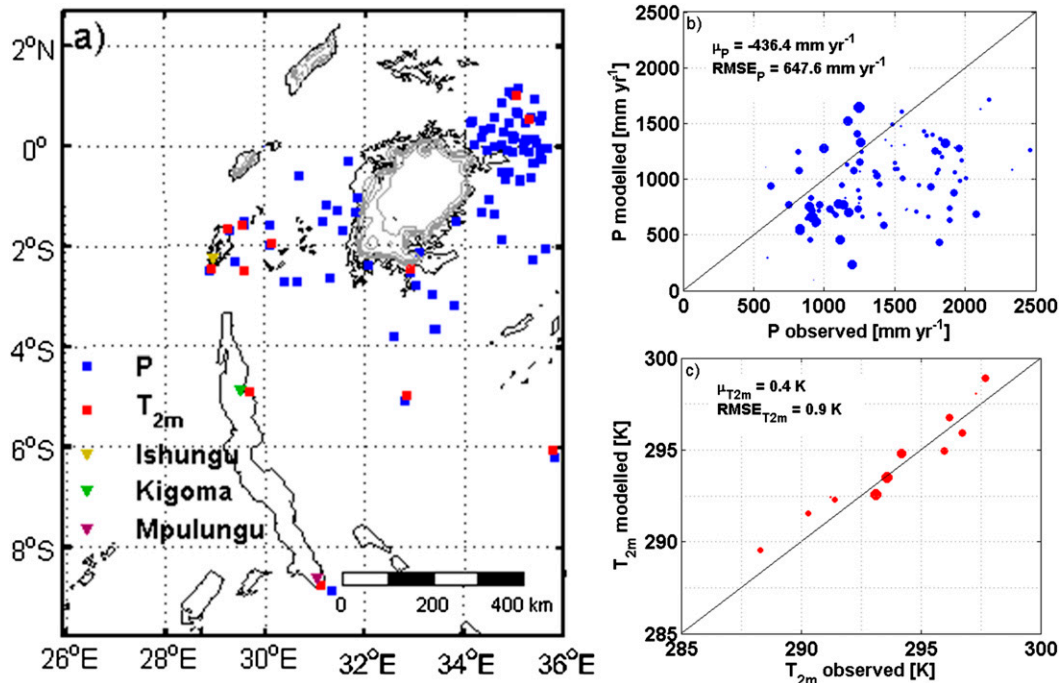
FIG. 4. (a) Map of in situ measurement locations of near-surface temperature T_{2m} (red squares) and precipitation P (blue squares), as well as three lake water temperature monitoring sites (colored triangles; see Fig. 6). Grey lines represent the bathymetry data (Kourzeneva et al. 2012) employed for the COSMO-CLM^2 CTL simulation (10-m equidistance and lake depths capped at 50 m, resulting in the absence of contours for several deep lakes). Scatter plots of modeled vs observed mean (b) P (mm yr^{-1}) and (c) T_{2m} (K). The variable μ presents the mean difference and RMSE of modeled vs observed P and T_{2m}, respectively. Data gaps in the observations were removed from the corresponding modelled time series. The size of the individual points reflects the availability of data during the analysis period (1999–2008) (the larger, the more data).

the observations and CTL, although precipitation is underestimated in April and during the main dry season. Multiyear monthly accumulated, domain-averaged precipitation biases against individual observational products are smaller than 90 mm month^{-1} during 90% of all months. Furthermore, monthly mean, domain-averaged modelled precipitation values are positively correlated with corresponding observations [significant ($p < 0.001$) Spearman rank correlation of 0.72, 0.85, 0.84, 0.80, and 0.84 with respect to TRMM 3B42, GPCC, GPCP, UDEL, and CMORPH, respectively].

Although very sparse, aggregated daily and monthly mean near-surface temperature observations in the region (T_{2m}) suggest the ability of COSMO-CLM^2 to reproduce spatial differences in T_{2m} (Fig. 4c). In addition, their annual cycle is well captured by COSMO-CLM^2, but the magnitude of the seasonality is slightly exaggerated by the model (not shown).

2) LAKE TEMPERATURE

COSMO-CLM^2 succeeds in reproducing the observed differences in LSWT among four major AGL but

demonstrates a slight warm bias for each of them (0.68 K on average; Figs. 5a–h; Table 2) and overestimates the amplitude of the seasonal LSWT cycle (Figs. 5i–l). Spatial LSWT patterns correspond to observations especially over Lake Victoria and Lake Tanganyika, with statistically significant spatial rank correlations of 0.68 and 0.61, respectively, and to a lesser extend over the other AGL. Over Lake Victoria, COSMO-CLM^2 suggests a positive temperature gradient from southwest to northeast, with a maximum temperature difference of 1 K. Although this modeled pattern is in contradiction with previous studies (e.g., Song et al. 2004; Anyah et al. 2006; Sun et al. 2014b,a), it matches with the spatial pattern derived from remote sensing (Figs. 5a,e), as well as with recent observations based on water temperature measurements at 48 locations during two cruises in February and August 2000 (MacIntyre et al. 2014). Unlike the observations, COSMO-CLM^2 furthermore predicts slightly higher lake surface temperatures in coastal zones and embayments as a result of the lower lake depths in these sectors.

The model's ability to reproduce lake surface temperatures is also apparent from the comparison between
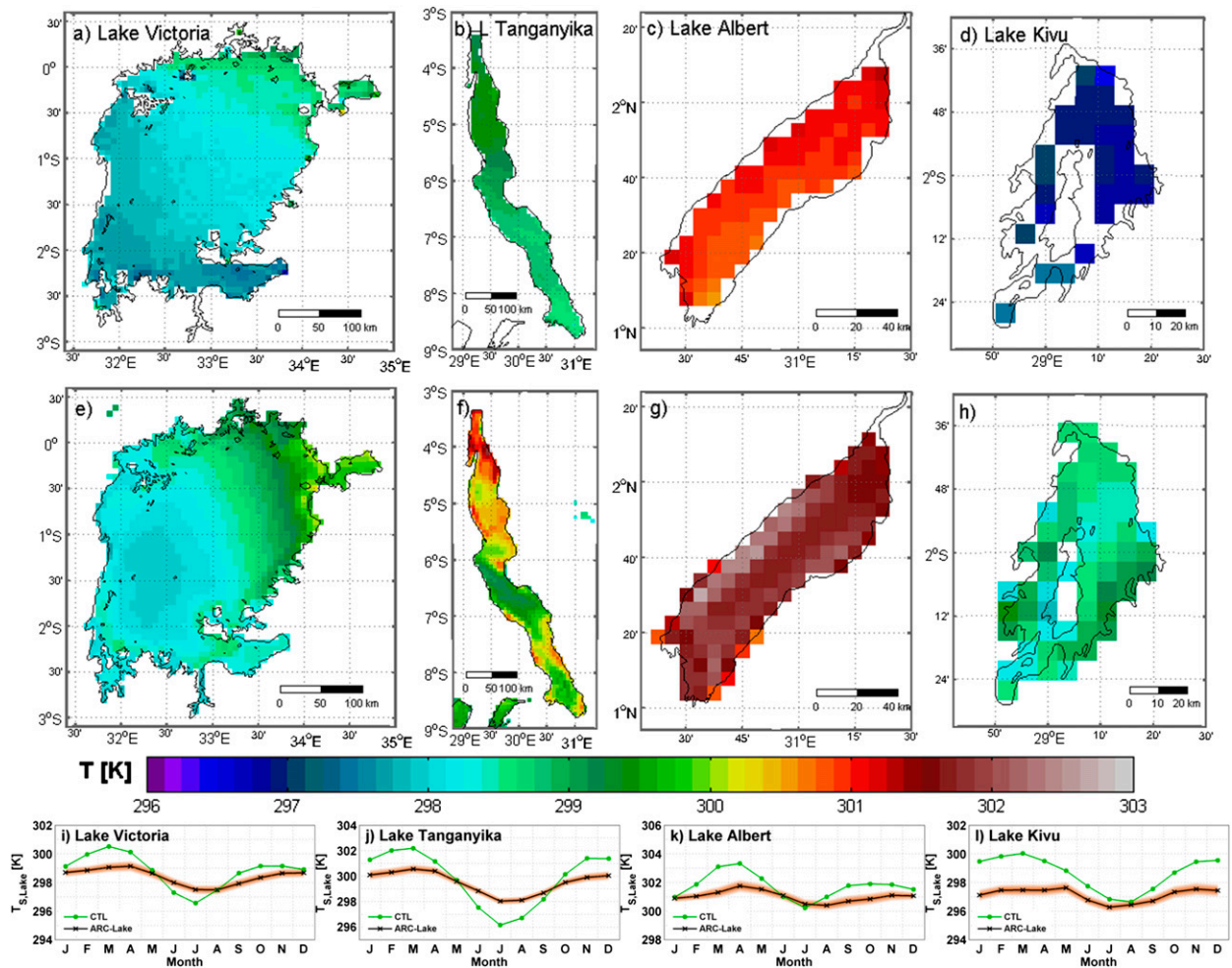
FIG. 5. The 1999–2008 (top) observed LSWT (K) from the ARC-Lake dataset and (middle) modeled LSWT from the COSMO-CLM²CTL simulation for (a),(e) Lake Victoria; (b),(f) Lake Tanganyika; (c),(g) Lake Kivu; and (d),(h) Lake Albert. (i)–(l) Lake-averaged observed (black line) and modeled (green line) monthly mean LSWT, including observational error estimate as provided with the product (red shading).

modeled and observed lake water temperatures at 0.5 m for three multiyear monitoring sites in Lake Kivu and Lake Tanganyika (Fig. 6). FLake reasonably predicts the annual mean 0.5-m lake temperature (with a warm bias of 1.23°, 0.71°, and 0.60°C at Ishungu, Kigoma, and Mpulungu, respectively) and reproduces the phase of the annual cycle but again exaggerates the amplitude of the seasonal temperature variations. Despite this overestimation, FLake captures the increasing seasonal cycle's amplitude with distance from the equator (Fig. 6). As this distance grows, the dry season becomes more pronounced, leading to a stronger evaporative-driven cooling of the lakes' mixed layer (Thiery et al. 2014a). Furthermore, interannual (near) surface lake temperature variability is present but can be considered small compared to the seasonal cycle. Observed anomalies

include the high temperatures during the 2005 long rains at Kigoma relative to the preceding months and the low temperatures during the 2007/08 stratified season at Ishungu (Figs. 6a,b). While the model reproduces the former warm anomaly at Kigoma, it does not predict the cold anomaly at Ishungu.

The overestimation of the annual LSWT cycle is primarily due to the underestimation of the mixed layer depth when stratified conditions are imposed in FLake (Thiery et al. 2014a). For a relatively shallow mixed layer, heat is concentrated in the top of the water column rather than being distributed over a larger volume. This, in turn, causes a stronger temperature response to seasonal changes in the lake's heat content and hence an overestimation of the annual LSWT cycle (Figs. 5i–l). Another potential cause for the remaining biases might

TABLE 2. Bias and spatial RMSE of COSMO-CLM^2, ERA-Interim, and the CORDEX parent simulation (section 2c) vs various observational products (see Table 1 for an overview).

Physical quantity (units)	COSMO-CLM^2		ERA-Interim		CORDEX	
	Bias	RMSE	Bias	RMSE	Bias	RMSE
TRMM 3B42 precipitation (mm yr^{-1})	−261	683	612	881	−717	838
GPCC precipitation (mm yr^{-1})	68	631	941	1160	−389	508
GPCP precipitation (mm yr^{-1})	30	554	903	1069	−427	519
UDEL precipitation (mm yr^{-1})	84	604	957	1167	−373	478
CMORPH precipitation (mm yr^{-1})	−330	712	739	907	−771	973
TRMM 2B31 precipitation (mm yr^{-1})	−273	678	599	873	−730	927
Ensemble precipitation* (mm yr^{-1})	−116	554	757	932	−573	669
GEWEX-SRB SW$_{net}$ (W m^{-2})	−12	22	39	42	−26	33
GEWEX-SRB LW$_{net}$ (W m^{-2})	−5	8	−21	24	1	7
LandFlux-EVAL LHF (W m^{-2})	−22	34	32	35	−27	31
FLUXNET-MTE SHF (W m^{-2})	10	22	−2	15	6	23
ISCCP CCF (%)	4	7	−1	6	3	6
ARC-Lake LSWT Victoria (K)	0.40	0.53	−4.16**	4.52**	−2.70	2.81
ARC-Lake LSWT Tanganyika (K)	1.09	1.16	−7.58**	7.82**	−3.07	3.35
ARC-Lake LSWT Albert (K)	0.90	0.94	—	—	−5.90	5.94
ARC-Lake LSWT Kivu (K)	1.80	1.83	—	—	−4.19	4.19

* Average of the six gridded precipitation products.
** Given the coarse resolution of this product and associated limited number of lake pixels, nearest neighbour interpolation was used in this case instead of bilinear interpolation.

be the role of three-dimensional water circulation within the larger lakes. For the relatively shallow Lake Victoria, Song et al. (2004) argue that an RCM coupled to a one-dimensional lake model reproduces first-order spatial lake surface temperature patterns but that only a three-dimensional lake model predicts a southwest–northeast heat transport within the lake. In the deep Lake Tanganyika, actual lake

hydrodynamics are still debated (e.g., Naithani et al. 2003; Verburg et al. 2011), but here variable wind forcing (Naithani et al. 2002), differential cooling (Verburg and Antenucci 2010; Verburg et al. 2011), water exchange across the thermocline (Gourgue et al. 2007), and internal Kelvin waves (Naithani and Deleersnijder 2004) may also eventually influence LSWT patterns. Further research could help to
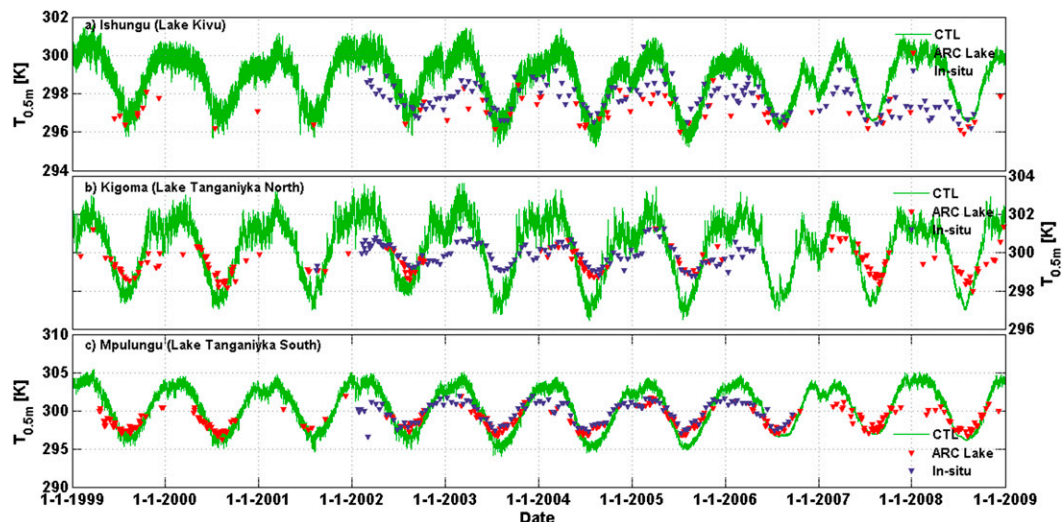

FIG. 6. Modeled (green lines), remotely sensed (ARC-Lake; red triangles) and bimonthly, in situ observed (blue triangles) lake temperatures (K) at (a) Ishungu (Lake Kivu; 2.34°S, 28.98°E), (b) Kigoma (Lake Tanganyika's northern basin; 4.85°S, 29.59°E), and (c) Mpulungu (Lake Tanganyika's southern basin; 8.73°S, 31.04°E) at a depth of 0.5 m (lake surface water temperatures in case of ARC-Lake).
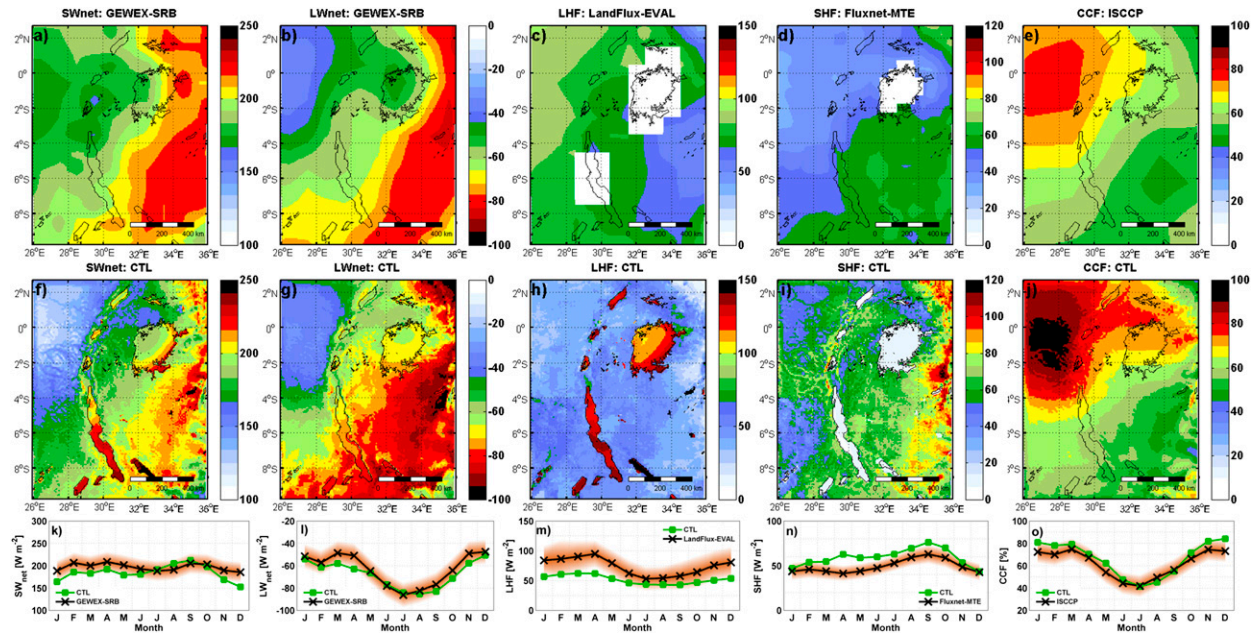
FIG. 7. (top) Observed and (middle) modeled annual mean maps and (bottom) domain-averaged seasonal cycles for (a),(f),(k) SW_{net} ($W\,m^{-2}$); (b),(g),(l) LW_{net} ($W\,m^{-2}$); (c),(h),(m) LHF ($W\,m^{-2}$); (d),(i),(n) SHF ($W\,m^{-2}$); and (e),(j),(o) CCF (%). The various observational products are described in Table 1, and both observational products and model output are shown for the respective measurement periods [(a),(e) 1999–2008; (b),(c) 1999–2007; and (d) 1999–2005]. For the white areas in (c) and (d), no data is available. The red shading around the observed annual cycle (black line) indicates the observational uncertainty as provided with the products.

discriminate the influence of lake hydrodynamics on lake–atmosphere exchanges for this region.

3) SURFACE ENERGY BALANCE AND CLOUDS

The ability of COSMO-CLM^2 to represent the surface climate is investigated by evaluating the surface energy fluxes. Good agreement is noted for the surface radiative fluxes, SW_{net} and LW_{net}, both in terms of spatial patterns and the domain-averaged annual cycle, indicating, among other things, the skill of CLM3.5 to simulate spatial and temporal albedo patterns over land (Figs. 7a,b,f,g,k,l). Modeled over-lake variations in SW_{net} (Fig. 7f) are due to spatial cloud cover variability, given the constant water surface albedo employed in FLake (0.07). Furthermore, very good agreement exists between the model and observations for cloud cover fraction (+4% bias; Figs. 7e,j,o; Table 2). The seasonal cycles of LW_{net} and CCF are strongly linked to each other and indicate more longwave radiative energy loss during the main dry season, when lower cloud cover fraction reduces the amount of incoming longwave radiation. During the short rains and the little dry season, a slight overestimation of CCF by ~8% induces a negative LW_{net} bias of $-5\,W\,m^{-2}$ during these months. Lower performance is noted for the turbulent fluxes, LHF and SHF ($-22\,W\,m^{-2}$ and $+10\,W\,m^{-2}$ bias, respectively; Figs. 7c,d,h,i,m,n; Table 2), with generally an

underestimation of LHF and an overestimation of SHF. Possibly, this overestimation of the Bowen ratio is caused by limited soil moisture availability, but given the lack of observational evidence, this is impossible to verify. Overall, domain-averaged monthly mean values for SW_{net}, LW_{net}, LHF, SHF, and CCF are within the observational uncertainty range during 10, 11, 7, 4, and 11 months of the year, respectively.

4) COMPARISON TO ERA-INTERIM AND CORDEX

To put the performance of the COSMO-CLM^2 CTL simulation into perspective, the same evaluation procedure was repeated for ERA-Interim and the COSMO-CLM CORDEX-Africa evaluation simulation (herein referred to as CORDEX; Panitz et al. 2014), each, respectively, representative of a state-of-the-art global reanalysis product and a continental-scale RCM simulation. Results indicate that COSMO-CLM^2 largely outperforms ERA-Interim for all considered variables, except for SHF and CCF, where both products depict similar skill (Table 2), and with the seasonal cycles of CCF mostly within the margins of observation uncertainty. Especially for precipitation and lake surface temperatures, COSMO-CLM^2 demonstrates remarkably lower biases and spatial root-mean-square errors (RMSE) compared to ERA-Interim. Relative to

the CORDEX simulation, the enhanced skill of COSMO-CLM^2 is also evident for P, SW$_{net}$, and LSWT, whereas LW$_{net}$, LHF, SHF, and CCF predictions demonstrate similar skill. Several effects are responsible for this enhanced skill. First, relatively few observations are assimilated into ERA-Interim over central Africa, leaving the model to run more freely over this region compared to other parts of the globe. Second, the use of a lake model clearly improves model performance relative to other common techniques, such as the sea surface temperature interpolation employed in ERA-Interim and CORDEX (Balsamo et al. 2012), for instance by reducing the absolute LSWT error over Lake Tanganyika by 86% and 65% relative to ERA-Interim and CORDEX, respectively (Table 2). Third, COSMO-CLM^2 benefits from the higher resolution relative to ERA-Interim and CORDEX (7 vs 79 and 50 km, respectively), allowing for more finescale circulation and associated precipitation patterns to develop over this complex terrain. Finally, the use of the Community Land Model improves the representation of the land surface albedo and other land surface characteristics relative to the default LSM of COSMO-CLM (Akkermans 2013).

In addition, the evaluation procedure was repeated for the NOL simulation, wherein lakes have been replaced by representative land pixels (see section 2c). The added value of the CTL simulation relative to NOL is apparent especially for precipitation and (lake) surface temperature (not shown). For precipitation, the enhanced skill of CTL can be attributed to the underestimation of the moisture input into the atmosphere in NOL (in the absence of lake evaporation), whereas an underestimation of surface thermal inertia deteriorates surface temperature variability in NOL.

In general, the evaluation results demonstrate that the near-surface climate is well represented by COSMO-CLM^2, the resolution is sufficient to capture effects of lakes and local orography on precipitation and other atmospheric variables, and the spatial and temporal patterns of the lake surface temperatures as well as differences between individual lakes are well represented by FLake. We therefore conclude that COSMO-CLM^2 is an appropriate tool to investigate the impact of the AGL on the regional climate.

b. Impact of the African Great Lakes on the regional climate

1) TEMPERATURE

Generally, the AGL clearly cool over-lake near-surface air (Table 3; Fig. 8), with average values of -0.67, -0.58, and -0.86 K for Lake Victoria, Lake Tanganyika and Lake Albert, respectively. Locally, the

TABLE 3. Impact of the African Great Lakes on different climatological values (CTL − NOL). ABS and REL denote the absolute and percentage change, respectively, of each given quantity, and * denotes the changes significant at the 5% significance level (two-tailed t test).

Physical quantity [Units]	All pixels		Lake pixels	
	ABS	REL	ABS	REL
Temperature at 2 m (K)	−0.17	−1	−0.57*	−2
Precipitation (mm yr^{-1})	59.10	5	712.77*	79
Surface temperature (K)	0.26	1	3.02*	13
Net SW radiation, surface (W m^{-2})	3.28*	2	30.63*	17
Net LW radiation, surface (W m^{-2})	−0.23	0	−4.95*	7
Latent heat flux (W m^{-2})	6.97	15	73.56*	142
Sensible heat flux (W m^{-2})	−4.34	−7	−52.36*	−85
Sea level pressure (hPa)	0.15	0	0.43*	0
Cloud cover fraction (%)	−0.05	0	−0.94	−1
evaporation (mm yr^{-1})	87.96	15	927.9*	142

cooling exceeds -1.5 K over each of these lakes, and -2 K over Lake Victoria. An interesting exception to this general pattern is Lake Kivu, where the lake presence induces an average warming of over-lake T_{2m} by $+0.75$ K relative to the NOL simulation. In section 3c, we further investigate causes of the temperature impact induced by the AGL.

Besides cooling the over-lake surfaces, the AGL also have a pronounced downwind influence on T_{2m}, as the cooler temperatures are advected by the daytime lake breeze into the adjacent land. This is especially visible north of Lake Victoria and around Lake Tanganyika and results in a domain-averaged cooling of -0.17 K. In contrast, the central part of the Albertine Rift mountains [e.g., Rwenzori (0.0°–0.8°N, 29.7°–30.2°E) and Virunga (1.3°–1.6°S, 29.1°–29.7°E) mountain ranges] block all near-surface atmospheric circulation and thereby constrain the influence of Lake Albert, Lake Edward, and Lake Kivu to their direct surroundings. Likewise, the steep topography surrounding Lake Tanganyika [e.g., Itombwe (2.5°–4.5°S, 28.5°–29.1°E), Kibira (2.2°–3.8°S, 29.1°–29.6°E), and Mahale (6.0°–6.5°S, 29.7°–30.1°E) Mountains] limits its cooling influence to the lower inland (Figs. 1, 8). The central plateau south of Lake Victoria is also not influenced by the lake presence, given the predominantly southeasterly flow in this part of the domain. These elements highlight that distance from the lake is not the only decisive factor determining the lake influence on T_{2m} but that topography and atmospheric circulation also play a major role.

The lake influence on T_{2m} is characterized by a clear seasonal pattern, with stronger cooling in the months following the main dry season (August–October: -1.4 K
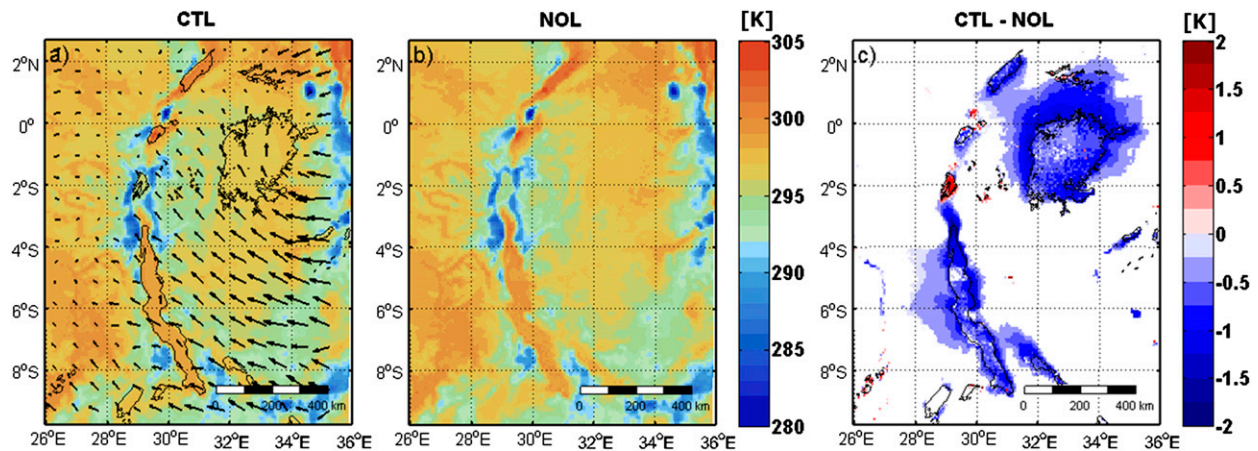
FIG. 8. Impact of the AGL on 2-m air temperature T_{2m}. Shown are annual mean T_{2m} (K) for the (a) CTL and (b) NOL simulations; (c) statistically significant changes at the 5% significance level (CTL − NOL; two-tailed t test) over the period 1999–2008. Temporally averaged 10-m wind vectors from the control simulation are shown in (a).

over the AGL vs −0.3 K during the remaining months; Figs. 10a,d), caused by seasonally variable land–water temperature contrasts. Near-surface water temperature variability in the AGL is primarily governed by LHF, for which the lake-induced change peaks during the main dry season (JJA; Figs. 10c,f) as near-surface relative humidity drops and induces the evaporative cooling of the lake surfaces (Savijärvi and Järvenoja 2000; MacIntyre 2012; Schmid and Wüest 2012; Thiery et al. 2014a). Land temperatures follow a similar seasonal pattern, but increase more rapidly at the end of the dry season because of their relatively low heat capacity. Hence, the largest land–lake temperature contrast and associated lake cooling effect is found from August to October. For similar reasons, the strongest AGL cooling occurs during daytime (0700–1600 UTC), because at

night lakes have a warming effect (1800–0500 UTC; Figs. 10g,j).

2) PRECIPITATION

As a result of the lakes' presence, modeled precipitation is enhanced by 59 mm yr^{-1} (+5%) on average over the model domain, by 713 mm yr^{-1} (+79%) over all lake pixels, and by 732 mm yr^{-1} (+87%) over the four major AGL (Table 3; Fig. 9). The largest increase is noted over Lake Kivu (+1373 mm yr^{-1} or +145%), whereas the three other major AGL induce similar absolute increases over their surface [+706 mm yr^{-1} (+85%), +745 mm yr^{-1} (+82%), and +647 mm yr^{-1} (+112%) over Lake Victoria, Lake Tanganyika, and Lake Albert, respectively]. The smaller lakes within the model domain generate similar increases, except for
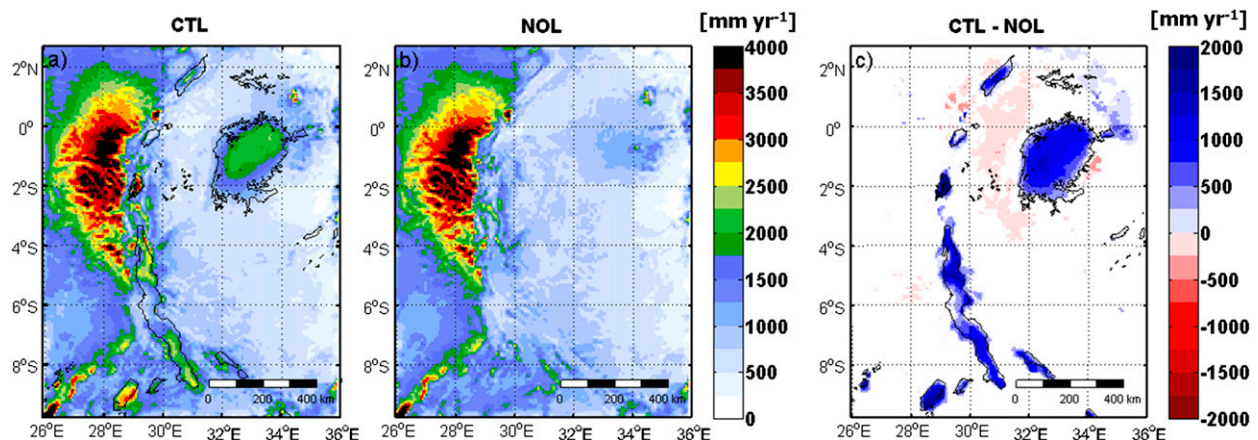

FIG. 9. Impact of the AGL on precipitation. Shown are annual mean P (mm yr^{-1}) for the (a) CTL and (b) NOL simulations; (c) statistically significant changes at the 5% significance level (CTL − NOL; two-tailed t test) over the period 1999–2008.

Lake Edward, which does not produce any additional precipitation according to COSMO-CLM^2.

In contrast to the influence of the lakes on T_{2m}, the precipitation impact is very localized and mostly limited to the lake itself (Fig. 9c). Over Lake Victoria, lake-induced precipitation increases from southeast to northwest, demonstrating the nonuniform response of the atmospheric column to the presence of the lake, in line with Anyah and Semazzi (2004). Over Lake Tanganyika, the increase in precipitation over the central part is absent or weak compared to the northern and southern sectors. In this part of the lake, a narrow corridor induces relatively strong dry season winds (see also Savijärvi and Järvenoja 2000), which transport over-lake air masses westward into the Congo basin (see also Fig. 8a). The differential spatial impact patterns confirm that next to changes in evapotranspiration, temporal patterns and changes in circulation induced by the AGL also play a dominant role in redistributing precipitation (Datta 1981; Savijärvi 1997; Savijärvi and Järvenoja 2000; Song et al. 2004; Anyah and Semazzi 2004; Anyah et al. 2006; Anyah and Semazzi 2007, 2009; Williams et al. 2015). Our findings furthermore suggest that onshore pluviometer measurements will never fully capture precipitation effects induced by the AGL. The dynamical response to lake presence is further investigated in section 3d.

Precipitation over the AGL displays a distinct diurnal cycle, with precipitation occurring mostly at night and morning hours over the lakes (0000–0900 UTC). This is in general agreement with observations from a pluviometer representative of the central Lake Victoria (Datta 1981). For the surrounding land, in contrast, the precipitation maximum occurs around local noon (0700–1200 UTC; Figs. 10h,k). The nighttime precipitation maximum is enabled by the sustained evaporation from the lakes throughout the whole day. This is not the case for the land evapotranspiration, which displays a clear maximum during the local afternoon and slightly lags the precipitation peak (Figs. 10i,l). Overall, the AGL generate a total moisture input into the atmosphere of 222 km^3 yr^{-1}, which is 134 km^3 yr^{-1} more than the equivalent land surface (+151%). This increase is more than sufficient to explain the enhanced over-lake precipitation production (+99 km^3 yr^{-1}), both on daily and subdaily time scales. On seasonal scales, the impact on precipitation is lowest during the main dry season (JJA: +7 mm month^{-1} over the AGL vs +77 mm month^{-1} during the remaining months).

c. Decomposing the lake-induced surface temperature change

An overview of the net changes in the main components of the surface energy balance induced by the lake presence, for all pixels and lake pixels only, is provided in Figs. 11a and 11c, respectively. The increase in net shortwave radiation (δSW$_{net}$) is caused by the lower albedo of water relative to the surrounding land (-0.12) and reduced cloud cover during daytime. Furthermore, as lakes evaporate at the potential evaporation rate, they enhance evapotranspiration (LHF) relative to the surrounding land, while SHF is reduced (Table 3).

The seven factors contributing to a change in surface temperature are described in Eq. (2) and are expressed in Kelvin. The parameters and flux components responsible for these forcings are shown with their corresponding forcing in Figs. 11b,d. Note that the temperature imbalance is only 0.005 and 0.002 K for the all-pixels and lake-pixels case, respectively, demonstrating balance closure for the depicted components.

Lakes are darker and therefore reflect less incoming radiation, resulting in a positive contribution to δT_s from changing albedo of $+0.51$ K over the whole domain and $+4.91$ K over the lakes (Figs. 11b,d: α). On the other hand, the contribution to δT_s caused by the higher surface longwave emissivity of water relative to the surrounding vegetation is negligible (Figs. 11b,d: ϵ). A strong increase in evaporation from the lakes contributes to a lower δT_s by -1.30 K over the whole domain and up to -12.21 K over the lakes and forms the largest individual contribution to δT_s (Figs. 11b,d: LHF). Note that, since the change in evapotranspiration is influenced by the latent heat of vaporization and air saturation (in turn, depending on temperature), it is impossible to distinguish between direct and indirect components in the case of LHF (Akkermans et al. 2014). The lower roughness length of the lake surface relative to vegetated land increases aerodynamic resistance and therefore slows down the turbulent heat transfer from the surface to the atmosphere. The upward SHF is also modified by a changing temperature gradient within the atmospheric surface layer. Together, both processes induce a warming of the surface by $+0.81$ K over the whole domain, and $+8.64$ K over the AGL, thereby presenting the strongest positive impact of T_s (Figs. 11b,d: SHF). Furthermore, since daytime cloud cover over the AGL is not significantly modified (+2%), the contribution of changing incoming shortwave radiation to δT_s is negligible over the AGL (Figs. 11b,d: SW$_{in}$). The same can be said for the contribution from changing incoming longwave radiation, a feedback depending both on cloud cover and atmospheric temperature (Figs. 11b,d: LW$_{in}$). Finally, the impact of a changing subsurface heat flux represents a small positive contribution to δT_s (Figs. 11b,d: G).

As expected, the temperature impact of lake presence is much larger over the AGL compared to the rest of the
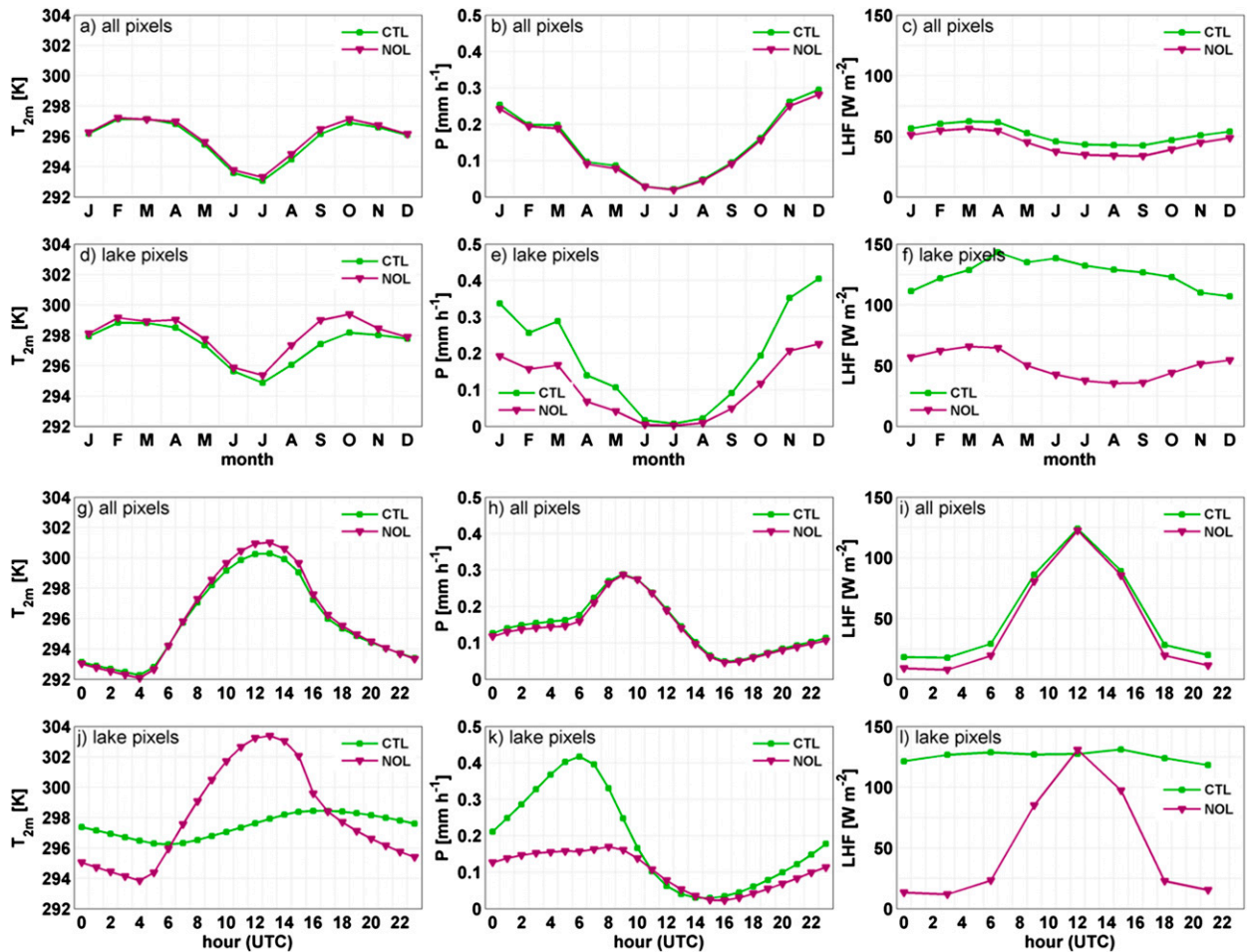
FIG. 10. Domain-averaged seasonal cycle over the period 1999–2008 for (a) T_{2m} (K), (b) P (mm h^{-1}), and (c) LHF (W m^{-2}) from the CTL and NOL simulations (green and purple lines, respectively). (d)–(f) As in (a)–(c), but considering only lake pixels in CTL and the corresponding pixels in NOL. (g)–(l) As in (a)–(f), but for the diurnal cycle.

domain (Table 3). However, due to the dynamical changes induced by the AGL and associated changes in near-surface temperature and moisture (see section 3d for a detailed description), some components are altered over land as well. For instance, the warming effect caused by the enhanced daytime incoming solar radiation (SW$_{in}$) becomes slightly more important when considering the whole domain, while the influence of a change in incoming longwave radiation (LW$_{in}$) switches sign (Figs. 11b,d).

Altogether, individual contributions to δT_s result in surface temperature increases of 0.26 and 3.02 K over the whole domain and the AGL, respectively (Figs. 11b,d; Table 3). This seems to be in contradiction with the simulated change in T_{2m}, which was shown to decrease on average (Figs. 8, 11b,d; Table 3). This apparent contradiction is, however, solved when comparing the forcing components separately during daytime (0900, 1200, 1500, and 1800 UTC) and nighttime (2100, 0000, 0300, and

0600 UTC; Fig. 12a). Note that the full surface energy balance decomposition method cannot be applied on subdaily time scales due to the lag effect of the heat storage component; hence, δG is computed from Eq. (2) in this case.

Although δT_s and δT_{2m} depict the same sign on subdaily time scales, their magnitudes vary. During daytime, both T_s and T_{2m} are lower in CTL relative to NOL, as a large fraction of the solar energy penetrates the lakes rather than being absorbed at the surface (Fig. 12a: G). At night, when this heat is released again from the mixed layer to the surface, the opposite effect is seen. The contribution of G to δT_s is only partly offset by reduced SHF during daytime and enhanced LHF during nighttime in CTL relative to NOL (Fig. 12a: SHF and LHF). Furthermore, the lake influence on vertical turbulent heat transport explains the differences in magnitude between δT_s and δT_{2m}: during daytime, the strong decrease in SHF over the lakes (shown by the strong
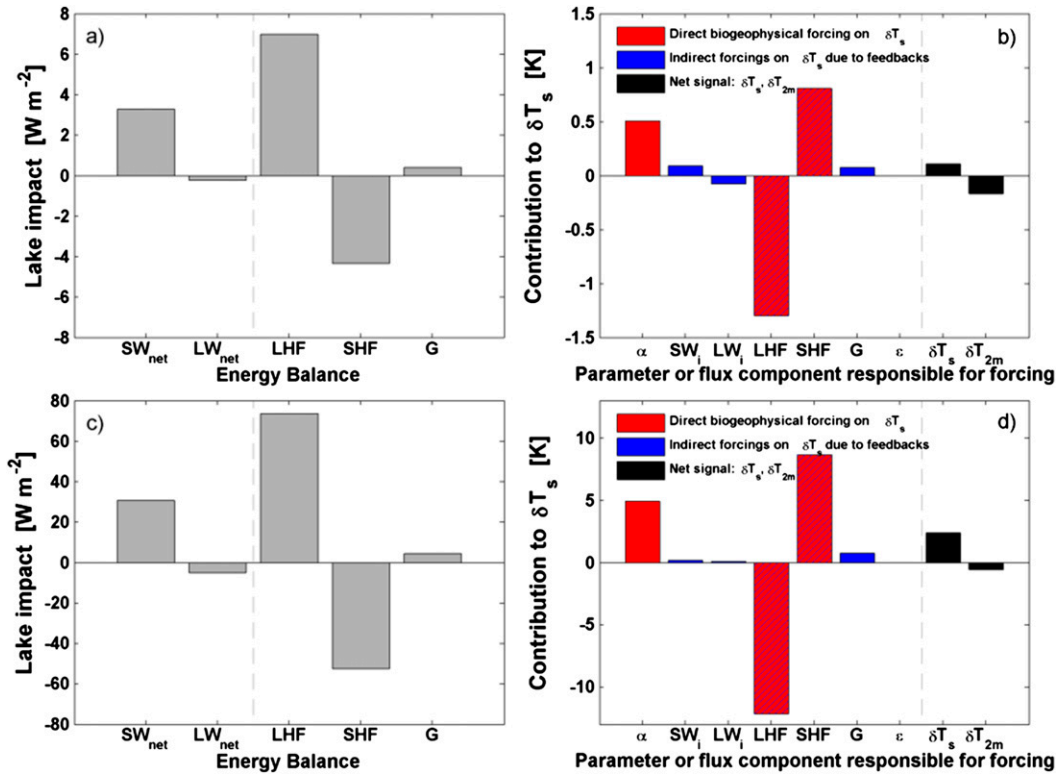
FIG. 11. Lake-induced change in the surface energy balance components SW$_{net}$, LW$_{net}$, LHF, SHF, and G for (a) the whole domain and (c) lake pixels only (all units W m^{-1}). Individual direct (red), indirect (blue), and mixed (hatched) contributions to δT_s described in Eq. (2) are shown for (b) the whole domain and (d) lake pixels only (all units K). Each contributing factor is indicated by its corresponding responsible parameter or flux component, with α denoting the change in T_s caused by a modified albedo, SW$_i$ by changing incoming shortwave radiation, LW$_i$ by changing incoming longwave radiation, LHF by changing evapotranspiration, SHF$_{res}$ by changing sensible heat flux due to modified aerodynamic resistance, SHF$_{tmp}$ by changing sensible heat flux due to temperature gradient, G by changing subsurface heat flux, and ϵ by changing emissivity. Finally, the AGL impact on T_{2m} is also shown.

positive contribution of SHF to δT_s in Fig. 12a) effectively inhibits heat transfer away from the surface—hence, the more pronounced decrease in T_{2m} relative to T_s. At night, the relative contribution to δT_s vanishes as

SHF drops over land while remaining more or less constant over lake surfaces (Fig. 12a), but again low SHF limits warming at 2 meters (see also Fig. 7i). Hence, when considering the whole day, the nighttime warming
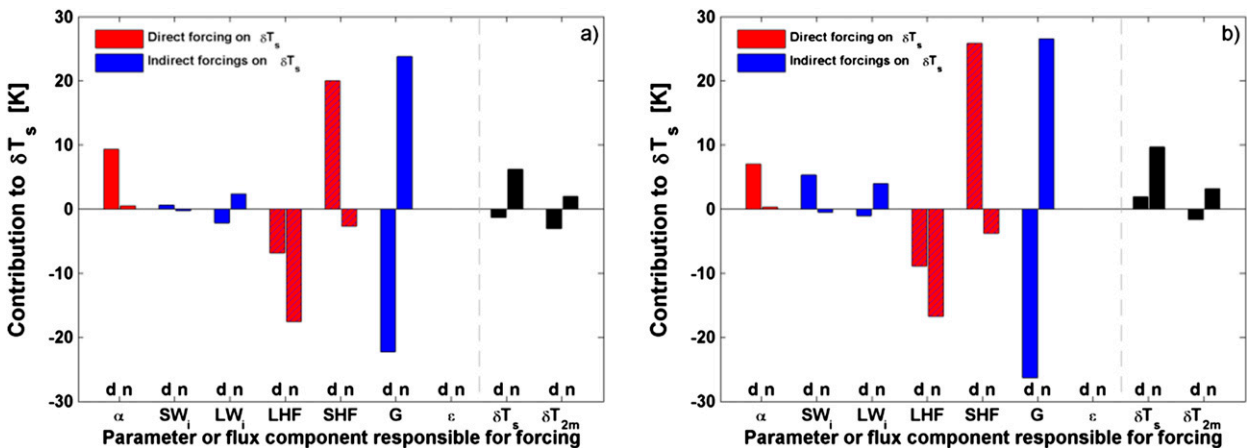

FIG. 12. (a) As in Fig. 11d, but now separately for 0900–1800 UTC (daytime; shown as d) and 2100–0600 UTC (nighttime; shown as n). (b) As in (a), but for Lake Kivu only.
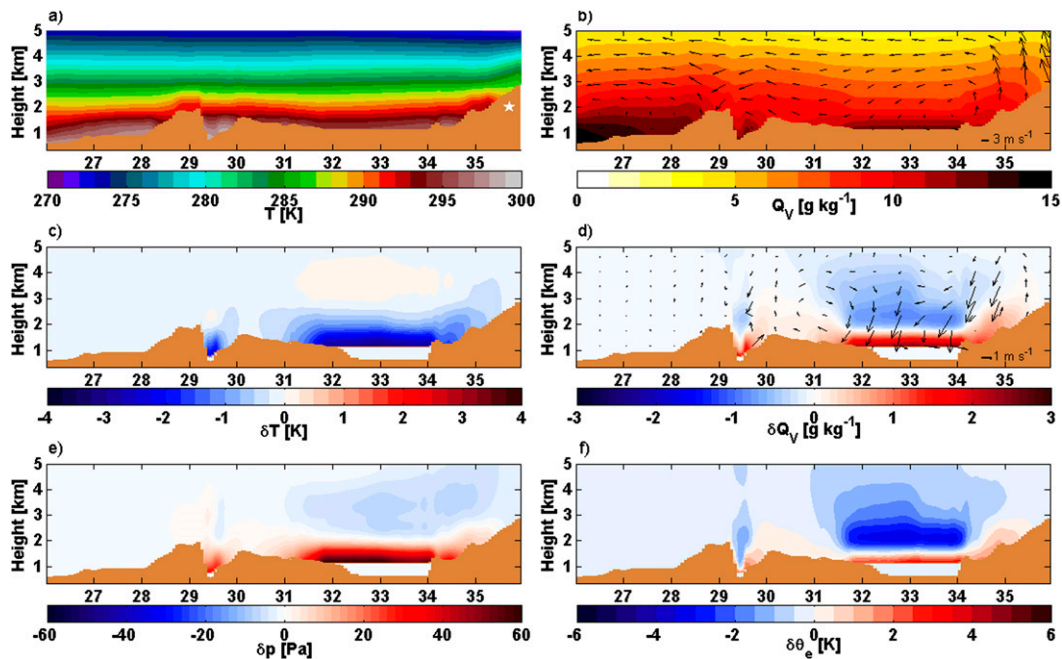
FIG. 13. Vertical cross sections along the transect indicated in Fig. 1 for the 10-yr reference climatologies (CTL, 1999–2008) from 0900–1800 UTC (daytime) of (a) T (K) and (b) Q_V (g kg^{-1}), including longitudinal circulation climatology, and for the mean change due to lake presence (CTL − NOL) in (c) δT (K); (d) δQ_V (g kg^{-1}) due to heat low-induced net convergence at lower levels, as indicated by arrows; (e) δp (Pa); and (f) e $\delta\theta_e$ (K). Lake depth and vertical wind velocity were height exaggerated by factor 10 and 200, respectively. The white star in (a) denotes the Kenyan Rift Valley mountains.

dominates δT_s, whereas the daytime cooling dominates δT_{2m} (Figs. 11d, 12a).

Lake Kivu constitutes an interesting exception, as argued in sections 3b(1) and 3b(2), given the positive T_{2m} anomaly and strong precipitation increase generated by its presence (Figs. 8, 9). The reasons for this behavior become apparent when applying the surface energy balance decomposition method to this lake alone. Over Lake Kivu, daytime T_s increases as SHF is strongly dampened during this time (+25.81 K contribution to δT_s; Fig. 12b). Furthermore, the lake presence lowers daytime cloud cover and therefore enhances solar radiation input. Both effects are only partly offset by changes in other contributions to δT_s (Fig. 12b: G, α, and LHF). At night, the heat release from Lake Kivu is modeled to be more effective relative to the other AGL, further strengthening the nighttime warming influence. The different response of the various surface energy balance components is likely caused by the high altitude of Lake Kivu (1463 m MSL) relative to other AGL. In our simulation, the surface layer over Lake Kivu is predicted to be very unstable, with an average 3.4-K temperature difference between the lake surface and 2-m level (relative to 1.7, 1 .7, and 1.2 K over Lake Victoria, Lake Tanganyika, and Lake Albert, respectively).

Overall, the absence of daytime T_s cooling and strong nighttime T_s warming in CTL relative to NOL causes Lake Kivu to display a general warming influence upon the near-surface air. In addition, the strong nighttime warming intensifies the dynamical response to lake presence (see also section 3d), leading to enhanced atmospheric column destabilization (Fig. 15b) and associated precipitation production.

d. Dynamical response to lake presence

The dynamical response of the atmosphere to lake presence is further investigated using a set of vertical cross sections along a transect covering the northern sector of Lake Victoria (Fig. 1). Based on the diurnal variability of lake impact on T_{2m} and precipitation (Figs. 10g–l), we construct two composites of the 1999–2008 3-hourly mean model output, with a first composite averaging output during daytime (0900, 1200, 1500, and 1800 UTC; Fig. 13) and a second during nighttime (2100, 0000, 0300, and 0600 UTC; Fig. 14).

During daytime, the atmospheric temperature decrease induced by the lake extends well beyond its shores and up to ~2-km height above the surface (Fig. 13c). At 2 km MSL, annual average daytime temperature still decreases by around −0.14 K over the
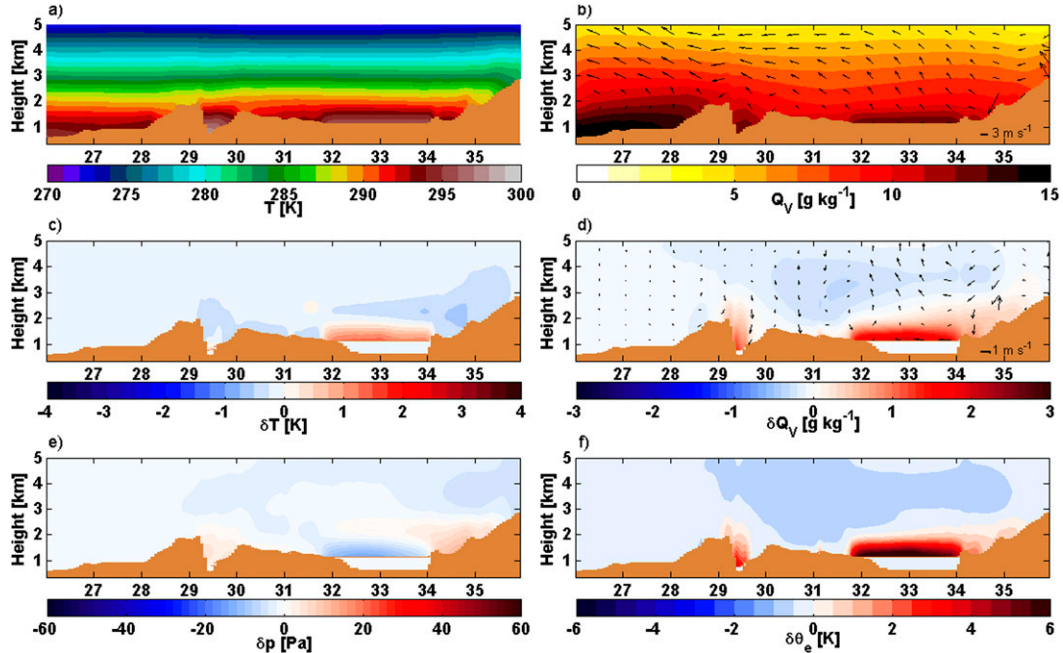
FIG. 14. As in Fig. 13, but from 2100–0600 UTC (nighttime).

whole model domain and by $-0.40\,\mathrm{K}$ over lake surfaces (both changes statistically significant at the 5% significance level). The pressure increase resulting from this cooling (in excess of $+0.60\,\mathrm{hPa}$; Fig. 13e) generates a lake breeze between ~1–2 km MSL across the lake shore towards the western rift valley (Fig. 13d). The lake breeze is offset by updrafts over land and with westerlies at ~3–5 km MSL and an over-lake, drying subsidence flow closing the secondary circulation cell over Lake Victoria's western sector (Fig. 13d). Although the moisture buildup in the persistently unstable surface layer (Verburg and Antenucci 2010) tends to destabilize the atmospheric column, the clockwise circulation induces a stabilization of the atmospheric column, especially over the western sector of the lake, as reflected by an increased equivalent potential temperature (θ_e) above ~1.5 km MSL and extending up to ~6 km MSL (Fig. 13f):

$$\theta_e = \left(T + \frac{L_v}{c_p} q_v \right) \left(\frac{p_0}{p} \right), \qquad (3)$$

where L_v is the latent heat of evaporation ($2.50 \times 10^6\,\mathrm{J\,kg^{-1}}$), c_p is the specific heat capacity of air at constant pressure ($1005\,\mathrm{J\,kg^{-1}\,K^{-1}}$), q_v is the specific humidity ($\mathrm{kg\,kg^{-1}}$), p_0 is the standard reference pressure ($1000 \times 10^2\,\mathrm{Pa}$), and p is the surface air pressure (Pa). The θ_e at lower levels enhances as the effect of increased humidity (Fig. 13d) overcompensates the effect of lower temperatures and higher air pressure (Figs. 13c,d). The

stabilization of the air results in a decrease in upward convective mass flux density (i.e. the vertical mass transport per unit area at cloud-base height due to convection; Fig. 15a), less intense convection, and, consequently, less rainfall during daytime over the lake. In contrast, the lake presence enhances the convective mass flux density during daytime around the lake (Fig. 15a) and therefore daytime precipitation.

In the eastern lake sector, the vicinity of the Kenyan Rift Valley mountains (Fig. 13a) modifies the classic lake-breeze circulation as observed over the western sector. Here, the primary daytime circulation is one of orographically induced convection (Fig. 13b), associated with an anabatic wind advecting the over-lake moisture upslope up to ~3 km MSL, confirming the conclusion from Anyah et al. (2006) that the anabatic daytime circulation is enhanced by the lake breeze. The strengthening of the anabatic component induces near-surface divergence and associated downward secondary flow aloft from ~2 to 5 km (Fig. 13d). Consequently, the primary upward motion is already suppressed onshore, causing less intense stabilization over the eastern sector relative to the western part (Figs. 13d,f) and consequently a more limited decrease in convective mass flux density (Fig. 15a).

At night, the lake surface warms the boundary layer and generates a statistically significant pressure deficit of about $-0.12\,\mathrm{hPa}$ at the surface (Figs. 14c,e). As a response, the secondary circulation over the western
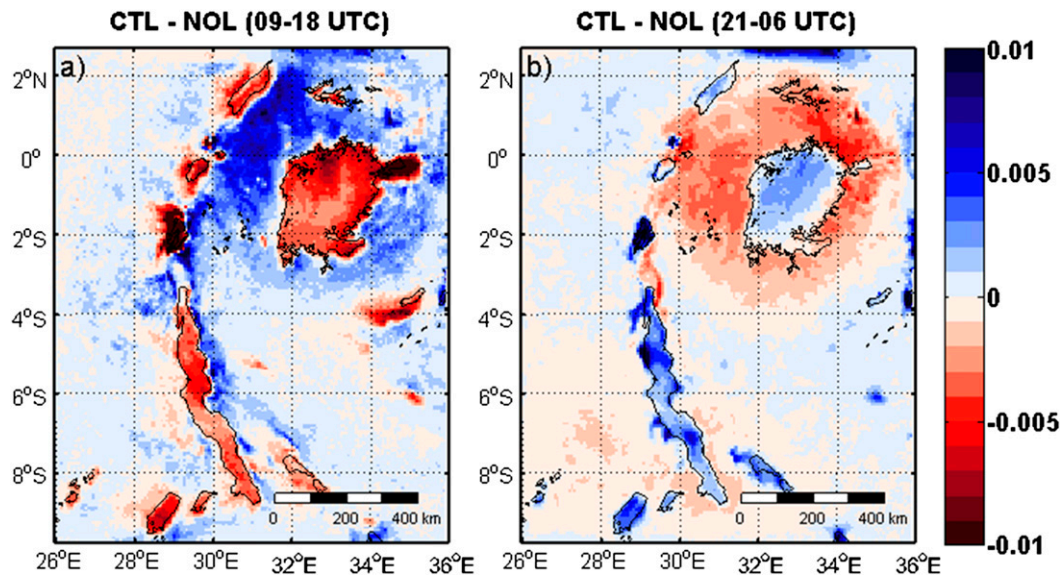
FIG. 15. The 1999–2008 mean change in convective mass flux density at cloud-base height ($kg\,m^{-2}\,s^{-1}$) induced by lake presence, for (a) 0900–1800 UTC (daytime) and (b) 2100–0600 UTC (nighttime).

sector is effectively reversed, with the lake breeze being replaced by a weak land breeze from the colder land to the warmer lake surface and offset by a counterclockwise motion aloft (Fig. 14d). When advected over the water, the cold air is warmed and moistened by strong evaporation from the lake (LHF ~100 $W\,m^{-2}$ higher than equivalent land points; Fig. 10l). While the near-surface air converges and induces upward motion, the warming signal dissipates more quickly in the vertical due to adiabatic decompression, and the enhanced moisture is efficiently transported aloft (Figs. 14c,d). At 1 km MSL, annual average nighttime specific humidity still increases by around +0.30 $g\,kg^{-1}$ over the whole domain and by +1.66 $g\,kg^{-1}$ over lake surfaces (both changes statistically significant at the 5% significance level). Also note that, again, this is the opposite of the daytime, when downward motion inhibits upward moisture transport building up in the boundary layer and rather transports it horizontally across the lake boundaries (Fig. 13d). At night, higher air temperatures, higher specific humidity, and lower air pressure reinforce each other in destabilizing the first ~1 km of the atmospheric column over Lake Victoria [see Eq. (3)], as reflected by the strong increase in θ_e there (~+6 K; Figs. 14c–f). This time, the increase of θ_e in lower levels is not accompanied by a notable decrease at higher levels caused by secondary circulation, pointing to the general destabilization of the nighttime over-lake atmospheric column. This, in turn, causes an increase in upward convective mass flux density (Fig. 15b), more intense convection, and associated precipitation during

nighttime over the lake. Again, the sign is reversed around the lake, where the lake presence reduces convection and, therefore, precipitation.

At night, the difference between the western and eastern sectors is generally less pronounced, although some differences can be noted. Over the eastern sector, the nighttime land breeze enforces katabatic winds flowing down from the eastern mountains (Anyah et al. 2006) and inhibits upslope transport of the warm temperature anomaly (Figs. 14b–d). The enhanced katabatic wind generates near-surface divergence on the eastern mountain slope and associated secondary downward motion aloft from ~2 to 4 km MSL, displaying similar secondary circulation over land compared to daytime, although less pronounced (Fig. 14d).

4. Conclusions

The influence of the AGL on the regional climate was studied for the period of 1999–2008 with the regional climate model COSMO-CLM[2]. Efforts were made to enhance the realism of the simulations by accounting for (i) a model setup and land surface model suited for tropical conditions; (ii) a horizontal grid resolution effectively resolving individual lakes and complex topography, unprecedented for climate simulations in this region; and (iii) a state-of-the-art one-dimensional lake model capable of reproducing tropical LSWT.

A comprehensive evaluation of COSMO-CLM[2], nested within the ERA-Interim-driven CORDEX-Africa simulation (COSMO-CLM), shows an adequate

representation of precipitation and LSWT; the model reproduces the most important spatial patterns, including enhanced over-lake precipitation, absolute LSWT values, and LSWT gradients within and between lakes. The phase and amplitude of the mean annual cycle are also similar to observations, although the amplitude is overestimated for LSWT, and precipitation is underestimated during April and the main dry season. The remaining LSWT biases are ascribed to an underestimation of the mixed layer depth and the absence of three-dimensional circulation in the larger lakes. Furthermore, the mean annual cycles of net shortwave and longwave radiation at the surface, sensible and latent heat flux, and cloud cover are mostly simulated within the margins of observational uncertainty. Finally, we show that our simulation largely outperforms a state-of-the-art reanalysis product (ERA-Interim) for most of the considered variables, especially precipitation and LSWT, whereas the added value relative to a state-of-the-art, continent-scale RCM simulation (COSMO-CLM CORDEX-Africa evaluation simulation) is evident for precipitation, LSWT, and net surface shortwave radiation.

The AGL significantly reduce offshore near-surface air temperature by about -0.57 K, with maxima in excess of -1.50 K. The cooling effect is advected across the lake shores within dynamic and orographic constraints and is found to be strongest at the end of the main dry season, when the land surface warms faster than the water surface and the lake–land temperature contrast reaches a maximum. The four major AGL also enhance precipitation by $+732$ mm yr^{-1} ($+87\%$) over their surface and even $+1373$ mm yr^{-1} ($+145\%$) over Lake Kivu. All lakes together annually evaporate 222 km^3 of water into the atmosphere. In contrast to the near-surface temperature impact, the precipitation change is highly restricted to the lake areas. Both for temperature and precipitation, the mean effect masks a pronounced diurnal pattern: the temperature signal exhibits strong cooling during daytime and moderate warming during nighttime over the lakes, whereas precipitation is enhanced mostly at night and during early morning.

Decomposition of the lake-induced surface temperature increase over the AGL shows that reduced albedo has a moderate warming influence ($+5.91$ K), while reduced sensible heating enhances surface temperatures even more ($+8.64$ K). For the most part, their effect is offset by the enhanced lake evaporation, responsible for -12.21 K cooling. The apparent contradiction between surface and near-surface temperature change is cleared by considering daytime and nighttime separately: daytime heat storage in the lake and reduced upward sensible heat flux dominate the near-surface air temperature

change, whereas the nighttime warming determines the surface temperature signal.

Finally, analysis of the dynamical response using daytime and nighttime cross sections over Lake Victoria highlights the importance of circulation changes induced by the lake–land temperature contrast. During daytime, the lake breeze transports cold air across the lake borders and generates overland updrafts and over-lake subsidence. This secondary circulation stabilizes the atmosphere above $\sim$1.5 km and therefore effectively suppresses convection from the unstable surface layer. At night, the thermal inertia of the lake surface generates a positive temperature anomaly and a pressure deficit and maintains the daytime evaporation rates, inputting large amounts of moisture into the boundary layer. These three effects together cause a strong destabilization of the lower atmosphere. As the land breeze and secondary circulation subsequently induce near-surface convergence and the lifting of these highly unstable air masses, strong convection is triggered, and precipitation is released over the lake. On the eastern shore, complex topography and associated gravity currents superimpose on this pattern, generating a somewhat different response, especially during daytime.

REFERENCES

Akkermans, T., 2013: Modeling land-atmosphere interactions in tropical Africa: The climatic impact of deforestation in the Congo Basin. Ph.D. thesis, KU Leuven, 160 pp.

——, and Coauthors, 2012: Validation and comparison of two soil–vegetation–atmosphere transfer models for tropical Africa. *J. Geophys. Res.,* **117,** G02013, doi:10.1029/2011JG001802.

——, W. Thiery, and N. P. M. Van Lipzig, 2014: The regional climate impact of a realistic future deforestation scenario in the Congo basin. *J. Climate,* **27,** 2714–2734, doi:10.1175/JCLI-D-13-00361.1.

Anyah, R. O., and F. H. M. Semazzi, 2004: Simulation of the sensitivity of Lake Victoria basin climate to lake surface temperatures. *Theor. Appl. Climatol.,* **79,** 55–69, doi:10.1007/s00704-004-0057-4.

——, and ——, 2006: Climate variability over the Greater Horn of Africa based on NCAR AGCM ensemble. *Theor. Appl. Climatol.,* **86,** 39–62, doi:10.1007/s00704-005-0203-7.

——, and ——, 2007: Variability of East African rainfall based on multiyear RegCM3 simulations. *Int. J. Climatol.,* **27,** 357–371, doi:10.1002/joc.1401.

——, and ——, 2009: Idealized simulation of hydrodynamic characteristics of Lake Victoria that potentially modulate regional climate. *Int. J. Climatol.,* **29,** 971–981, doi:10.1002/joc.1795.

——, ——, and L. Xie, 2006: Simulated physical mechanisms associated with climate variability over Lake Victoria basin in East Africa. *Mon. Wea. Rev.,* **134,** 3588–3609, doi:10.1175/MWR3266.1.

Argent, R., X. Sun, F. H. M. Semazzi, L. Xie, and B. Liu, 2015: The development of a customization framework for the WRF Model over the Lake Victoria basin, Eastern Africa on seasonal timescales. *Adv. Meteorol.,* **2015,** 653473, doi:10.1155/2015/653473.

Balsamo, G., R. Salgado, E. Dutra, S. Boussetta, T. Stockdale, and M. Potes, 2012: On the contribution of lakes in predicting near-surface temperature in a global weather forecasting model. *Tellus,* **64A,** 15829, doi:10.3402/tellusa.v64i0.15829.

Bates, G., S. Hostetler, and F. Giorgi, 1995: Two-year simulation of the Great Lakes region with a coupled modeling system. *Mon. Wea. Rev.,* **123,** 1505–1522, doi:10.1175/1520-0493(1995)123<1505:TYSOTG>2.0.CO;2.

Bennington, V., M. Notaro, and K. D. Holman, 2014: Improving climate sensitivity of deep lakes within a regional climate model and its impact on simulated climate. *J. Climate,* **27,** 2886–2911, doi:10.1175/JCLI-D-13-00110.1.

Bonan, G. B., 1995: Sensitivity of a GCM simulation to inclusion of inland water surfaces. *J. Climate,* **8,** 2691–2704, doi:10.1175/1520-0442(1995)008<2691:SOAGST>2.0.CO;2.

——, K. W. Oleson, M. Vertenstein, S. Levis, X. Zeng, Y. Dai, R. E. Dickinson, and Z.-L. Yang, 2002: The land surface climatology of the Community Land Model coupled to the NCAR Community Climate Model. *J. Climate,* **15,** 3123–3149, doi:10.1175/1520-0442(2002)015<3123:TLSCOT>2.0.CO;2.

Bookhagen, B., and D. W. Burbank, 2006: Topography, relief, and TRMM-derived rainfall variations along the Himalaya. *Geophys. Res. Lett.,* **33,** L08405, doi:10.1029/2006GL026037.

——, and M. R. Strecker, 2008: Orographic barriers, high-resolution TRMM rainfall, and relief variations along the eastern Andes. *Geophys. Res. Lett.,* **35,** L06403, doi:10.1029/2007GL032011.

Burbank, D. W., B. Bookhagen, E. J. Gabet, and J. Putkonen, 2012: Modern climate and erosion in the Himalaya. *C. R. Geosci.,* **344,** 610–626, doi:10.1016/j.crte.2012.10.010.

Climate Prediction Center, 2011: NOAA CPC Morphing Technique (CMORPH) Global Precipitation Analyses. Research Data Archive at the National Center for Atmospheric Research, Computational and Information Systems Laboratory, accessed 13 June 2014. [Available online at http://rda.ucar.edu/datasets/ds502.0/.]

Coe, M., and G. Bonan, 1997: Feedbacks between climate and surface water in northern Africa during the middle Holocene. *J. Geophys. Res.,* **102,** 11 087–11 101, doi:10.1029/97JD00343.

Crétat, J., E. K. Vizy, and K. H. Cook, 2014: How well are daily intense rainfall events captured by current climate models over Africa? *Climate Dyn.,* **42,** 2691–2711, doi:10.1007/s00382-013-1796-7.

Darchambeau, F., H. Sarmento, and J.-P. Descy, 2014: Primary production in a tropical large lake: The role of phytoplankton composition. *Sci. Total Environ.,* **473–474,** 178–188, doi:10.1016/j.scitotenv.2013.12.036.

Datta, R. K., 1981: Certain aspects of monsoonal precipitation dynamics over Lake Victoria. *Monsoon Dynamics,* J. Lighthill and R. P. Pearce, Eds., Cambridge University Press, 333–349.

Davies, H., 1983: Limitations of some common lateral boundary schemes used in regional NWP models. *Mon. Wea. Rev.,* **111,** 1002–1012, doi:10.1175/1520-0493(1983)111<1002:LOSCLB>2.0.CO;2.

Davin, E. L., and S. I. Seneviratne, 2012: Role of land surface processes and diffuse/direct radiation partitioning in simulating the European climate. *Biogeosciences,* **9,** 1695–1707, doi:10.5194/bg-9-1695-2012.

——, R. Stöckli, E. B. Jaeger, S. Levis, and S. I. Seneviratne, 2011: COSMO-CLM^2: A new version of the COSMO-CLM model coupled to the Community Land Model. *Climate Dyn.,* **37,** 1889–1907, doi:10.1007/s00382-011-1019-z.

——, S. I. Seneviratne, P. Ciais, A. Olioso, and T. Wang, 2014: Preferential cooling of hot extremes from cropland albedo management. *Proc. Natl. Acad. Sci. USA,* **111,** 9757–9761, doi:10.1073/pnas.1317323111.

De Boor, C., 1978: *A Practical Guide to Splines.* Applied Mathematical Sciences, Vol. 27, Springer-Verlag, 348 pp.

Dee, D. P., and Coauthors, 2011: The ERA-Interim reanalysis: Configuration and performance of the data assimilation system. *Quart. J. Roy. Meteor. Soc.,* **137,** 553–597, doi:10.1002/qj.828.

Dinku, T., S. Chidzambwa, P. Ceccato, S. J. Connor, and C. F. Ropelewski, 2008: Validation of high-resolution satellite rainfall products over complex terrain. *Int. J. Remote Sens.,* **29,** 4097–4110, doi:10.1080/01431160701772526.

Doms, G., 2011: A description of the nonhydrostatic regional COSMO-Model. Part I: Dynamics and numerics. COSMO Tech. Rep., 153 pp. [Available online at http://www.cosmo-model.org/content/model/documentation/core/cosmoDyncsNumcs.pdf.]

——, and Coauthors, 2011: A description of the nonhydrostatic regional COSMO Model. Part II: Physical parameterization. COSMO Tech. Rep., 161 pp. [Available online at http://www.cosmo-model.org/content/model/documentation/core/cosmoPhysParamtr.pdf.]

Dosio, A., H.-J. Panitz, M. Schubert-Frisius, and D. Lüthi, 2015: Dynamical downscaling of CMIP5 global circulation models over CORDEX-Africa with COSMO-CLM: Evaluation over the present climate and analysis of the added value. *Climate Dyn.,* **44,** 2637–2661, doi:10.1007/s00382-014-2262-x.

Endris, H. S., and Coauthors, 2013: Assessment of the performance of CORDEX regional climate models in simulating East African rainfall. *J. Climate,* **26,** 8453–8475, doi:10.1175/JCLI-D-12-00708.1.

Giorgi, F., C. Jones, and G. Asrar, 2009: Addressing climate information needs at the regional level: the CORDEX framework. *WMO Bull.,* **58,** 175–183.

Gourgue, O., E. Deleersnijder, and L. White, 2007: Toward a generic method for studying water renewal, with application to the epilimnion of Lake Tanganyika. *Estuarine Coastal Shelf Sci.,* **74,** 628–640, doi:10.1016/j.ecss.2007.05.009.

Goyens, C., D. Lauwaet, M. Schröder, M. Demuzere, and N. P. M. Van Lipzig, 2012: Tracking mesoscale convective systems in the Sahel: Relation between cloud parameters and precipitation. *Int. J. Climatol.,* **32,** 1921–1934, doi:10.1002/joc.2407.

Goyette, S., N. McFarlane, and G. M. Flato, 2000: Application of the Canadian regional climate model to the Laurentian great lakes region: Implementation of a lake model. *Atmos.–Ocean,* **38,** 481–503, doi:10.1080/07055900.2000.9649657.

Grasselt, R., D. Schüttemeyer, K. Warrach-Sagi, F. Ament, and C. Simmer, 2008: Validation of TERRA-ML with discharge measurements. *Meteor. Z.,* **17,** 763–773, doi:10.1127/0941-2948/2008/0334.

Gu, H., J. Jin, Y. Wu, M. B. Ek, and Z. M. Subin, 2015: Calibration and validation of lake surface temperature simulations with the coupled WRF-lake model. *Climatic Change,* **129,** 471–483, doi:10.1007/s10584-013-0978-y.

Gula, J., and W. R. Peltier, 2012: Dynamical downscaling over the Great Lakes basin of North America using the WRF Regional Climate Model: The impact of the Great Lakes system on regional greenhouse warming. *J. Climate,* **25,** 7723–7742, doi:10.1175/JCLI-D-11-00388.1.

Hernández-Díaz, L., R. Laprise, L. Sushama, A. Martynov, K. Winger, and B. Dugas, 2013: Climate simulation over CORDEX Africa domain using the fifth-generation Canadian Regional Climate Model (CRCM5). *Climate Dyn.,* **40,** 1415–1433, doi:10.1007/s00382-012-1387-z.

Hostetler, S. W., and F. Giorgi, 1995: Effects of a $2 \times CO_2$ climate on two large lake systems: Pyramid Lake, Nevada, and Yellowstone Lake, Wyoming. *Global Planet. Change,* **10,** 43–54, doi:10.1016/0921-8181(94)00019-A.

——, ——, G. T. Bates, and P. J. Bartlein, 1994: Lake–atmosphere feedbacks associated with paleolakes Bonneville and Lahontan. *Science,* **263,** 665–668, doi:10.1126/science.263.5147.665.

Huffman, G., R. Adler, M. Morrissey, D. Bolvin, S. Curtis, R. Joyce, B. McGavock, and J. Susskind, 2001: Global precipitation at one-degree daily resolution from multisatellite observations. *J. Hydrometeor.,* **2,** 36–50, doi:10.1175/1525-7541(2001)002<0036:GPAODD>2.0.CO;2.

Jacobs, L., O. Dewitte, J. Poesen, D. Delvaux, W. Thiery, and M. Kervyn, 2015: The Rwenzori Mountains, a landslide-prone region? *Landslides,* in press.

Joyce, R., J. Janowiak, P. Arkin, and P. Xie, 2004: CMORPH: A method that produces global precipitation estimates from passive microwave and infrared data at high spatial and temporal resolution. *J. Hydrometeor.,* **5,** 487–503, doi:10.1175/1525-7541(2004)005<0487:CAMTPG>2.0.CO;2.

Juang, J.-Y., G. Katul, M. Siqueira, P. Stoy, and K. Novick, 2007: Separating the effects of albedo from eco-physiological changes on surface temperature along a successional chronosequence in the southeastern United States. *Geophys. Res. Lett.,* **34,** L21408, doi:10.1029/2007GL031296.

Jung, M., M. Reichstein, and A. Bondeau, 2009: Towards global empirical upscaling of FLUXNET eddy covariance observations: Validation of a model tree ensemble approach using a biosphere model. *Biogeosciences,* **6,** 2001–2013, doi:10.5194/bg-6-2001-2009.

——, and Coauthors, 2010: Recent decline in the global land evapotranspiration trend due to limited moisture supply. *Nature,* **467,** 951–954, doi:10.1038/nature09396.

Kitaigorodskii, S. A., and Y. Z. Miropolskii, 1970: On the theory of the open ocean active layer. *Izv., Atmos. Ocean. Phys.,* **6,** 97–102.

Kourzeneva, E., 2010: External data for lake parameterization in Numerical Weather Prediction and climate modeling. *Boreal Environ. Res.,* **15,** 165–177.

——, H. Asensio, E. Martin, and S. Faroux, 2012: Global gridded dataset of lake coverage and lake depth for use in numerical weather prediction and climate modelling. *Tellus,* **64A,** 15640, doi:10.3402/tellusa.v64i0.15640.

Kummerow, C., and Coauthors, 2000: The status of the Tropical Rainfall Measuring Mission (TRMM) after two years in orbit. *J. Appl. Meteor.,* **39,** 1965–1982, doi:10.1175/1520-0450(2001)040<1965:TSOTTR>2.0.CO;2.

Laprise, R., and Coauthors, 2008: Challenging some tenets of regional climate modelling. *Meteor. Atmos. Phys.,* **100,** 3–22, doi:10.1007/s00703-008-0292-9.

——, L. Hernández-Díaz, K. Tete, L. Sushama, L. Šeparović, A. Martynov, K. Winger, and M. Valin, 2013: Climate projections over CORDEX Africa domain using the fifth-generation Canadian Regional Climate Model (CRCM5). *Climate Dyn.,* **41,** 3219–3246, doi:10.1007/s00382-012-1651-2.

Lauwaet, D., N. P. M. Lipzig, and K. Ridder, 2009: The effect of vegetation changes on precipitation and Mesoscale Convective Systems in the Sahel. *Climate Dyn.,* **33,** 521–534, doi:10.1007/s00382-009-0539-2.

——, N. P. M. van Lipzig, K. Van Weverberg, K. De Ridder, and C. Goyens, 2012: The precipitation response to the desiccation of Lake Chad. *Quart. J. Roy. Meteor. Soc.,* **138,** 707–719, doi:10.1002/qj.942.

Legates, D., and C. Willmott, 1990: Mean seasonal and spatial variability in gauge-corrected, global precipitation. *Int. J. Climatol.,* **10,** 111–127, doi:10.1002/joc.3370100202.

Lejeune, Q., E. Davin, B. Guillod, and S. Seneviratne, 2015: Influence of Amazonian deforestation on the future evolution of regional surface fluxes, circulation, surface temperature and precipitation. *Climate Dyn.,* **44,** 2769–2786, doi:10.1007/s00382-014-2203-8.

Lorenz, R., E. L. Davin, and S. I. Seneviratne, 2012: Modeling land-climate coupling in Europe: Impact of land surface representation on climate variability and extremes. *J. Geophys. Res.,* **117,** D20109, doi:10.1029/2012JD017755.

Luyssaert, S., and Coauthors, 2014: Land management and land-cover change have impacts of similar magnitude on surface temperature. *Nat. Climate Change,* **4,** 389–393, doi:10.1038/nclimate2196.

MacCallum, S., and C. Merchant, 2012: Surface water temperature observations of large lakes by optimal estimation. *Can. J. Remote Sens.,* **38,** 25–45, doi:10.5589/m12-010.

MacIntyre, S., 2012: Climatic variability, mixing dynamics, and ecological consequences in the African Great Lakes. *Climatic Change and Global Warming of Inland Waters: Impacts and Mitigation for Ecosystems and Societies,* C. R. Goldman, M. Kumagai, and R. D. Robarts, Eds., John Wiley & Sons, Inc., 311–337, doi:10.1002/9781118470596.ch18.

——, J. R. Romero, G. M. Silsbe, and B. M. Emery, 2014: Stratification and horizontal exchange in Lake Victoria, East Africa. *Limnol. Oceanogr.,* **59,** 1805–1838, doi:10.4319/lo.2014.59.6.1805.

Martynov, A., L. Sushama, R. Laprise, K. Winger, and B. Dugas, 2012: Interactive lakes in the Canadian Regional Climate Model, version 5: The role of lakes in the regional climate of North America. *Tellus,* **64A,** 16226, doi:10.3402/tellusa.v64i0.16226.

Mironov, D. V., 2008: Parameterization of lakes in numerical weather prediction. Part 1: Description of a lake model. COSMO Tech. Rep. 11, 47 pp. [Available online at http://www.cosmo-model.org/content/model/documentation/techReports/docs/techReport11.pdf.]

——, E. Heise, E. Kourzeneva, B. Ritter, N. Schneider, and A. Terzhevik, 2010: Implementation of the lake parameterisation scheme FLake into the numerical weather prediction model COSMO. *Boreal Environ. Res.,* **15,** 218–230.

Mueller, B., and Coauthors, 2013: Benchmark products for land evapotranspiration: LandFlux-EVAL multi-data set synthesis. *Hydrol. Earth Syst. Sci.,* **17,** 3707–3720, doi:10.5194/hess-17-3707-2013.

Naithani, J., and E. Deleersnijder, 2004: Are there internal Kelvin waves in Lake Tanganyika? *Geophys. Res. Lett.,* **31,** L06303, doi:10.1029/2003GL019156.

——, ——, and P.-D. Plisnier, 2002: Origin of intraseasonal variability in Lake Tanganyika. *Geophys. Res. Lett.,* **29,** 2093, doi:10.1029/2002GL015843.

——, ——, and ——, 2003: Analysis of wind-induced thermocline oscillations of Lake Tanganyika. *Environ. Fluid Mech.,* **3,** 23–39, doi:10.1023/A:1021116727232.

Nicholson, S., 1996: A review of climate dynamics and climate variability in Eastern Africa. *The Limnology, Climatology and Paleoclimatology of the East African Lakes,* T. Johnson and E. Odada, Eds., CRC Press, 25–56.

Nikulin, G., and Coauthors, 2012: Precipitation climatology in an ensemble of CORDEX-Africa regional climate simulations. *J. Climate,* **25,** 6057–6078, doi:10.1175/JCLI-D-11-00375.1.

Notaro, M., K. Holman, A. Zarrin, E. Fluck, S. Vavrus, and V. Bennington, 2013: Influence of the Laurentian Great Lakes on regional climate. *J. Climate,* **26,** 789–804, doi:10.1175/JCLI-D-12-00140.1.

Nyeko-Ogiramoi, P., G. Ngirane-Katashaya, P. Willems, and V. Ntegeka, 2010: Evaluation and inter-comparison of Global Climate Models' performance over Katonga and Ruizi catchments in Lake Victoria basin. *Phys. Chem. Earth,* **35,** 618–633, doi:10.1016/j.pce.2010.07.037.

——, P. Willems, and G. Ngirane-Katashaya, 2013: Trend and variability in observed hydrometeorological extremes in the Lake Victoria basin. *J. Hydrol.,* **489,** 56–73, doi:10.1016/j.jhydrol.2013.02.039.

Oleson, K. W., and Coauthors, 2004: Technical description of the Community Land Model (CLM). NCAR Tech. Note NCAR/TN-461+STR, 186 pp., doi:10.5065/D6N877R0.

——, and Coauthors, 2008: Improvements to the Community Land Model and their impact on the hydrological cycle. *J. Geophys. Res.,* **113,** G01021, doi:10.1029/2007JG000563.

Panitz, H.-J., A. Dosio, M. Büchner, D. Lüthi, and K. Keuler, 2014: COSMO-CLM (CCLM) climate simulations over CORDEX-Africa domain: Analysis of the ERA-Interim driven simulations at 0.44° and 0.22° resolution. *Climate Dyn.,* **42,** 3015–3038, doi:10.1007/s00382-013-1834-5.

Perroud, M., and S. Goyette, 2009: Simulation of multiannual thermal profiles in deep Lake Geneva: A comparison of one-dimensional lake models. *Limnol. Oceanogr.,* **54,** 1574–1594, doi:10.4319/lo.2009.54.5.1574.

Plisnier, P.-D., S. Serneels, and E. Lambin, 2000: Impact of ENSO on East African ecosystems: A multivariate analysis based on climate and remote sensing data. *Global Ecol. Biogeogr.,* **9,** 481–497, doi:10.1046/j.1365-2699.2000.00208.x.

——, and Coauthors, 2009: Limnological variability and pelagic fish abundance (*Stolothrissa tanganicae* and *Lates stappersii*) in Lake Tanganyika. *Hydrobiologia,* **625,** 117–134, doi:10.1007/s10750-009-9701-4.

Raschendorfer, M., 2001: The new turbulence parameterization of LM. *COSMO newsletter,* No. 1, Deutscher Wetterdienst, Offenbach, Germany, 90–98. [Available online at http://cosmo-model.cscs.ch/content/model/documentation/newsLetters/newsLetter01/newsLetter_01.pdf.]

Read, J. S., and Coauthors, 2012: Lake-size dependency of wind shear and convection as controls on gas exchange. *Geophys. Res. Lett.,* **39,** L09405, doi:10.1029/2012GL051886.

Ritter, B., and J. Geleyn, 1992: A comprehensive radiation scheme for numerical weather prediction models with potential applications in climate simulations. *Mon. Wea. Rev.,* **120,** 303–325, doi:10.1175/1520-0493(1992)120<0303:ACRSFN>2.0.CO;2.

Rockel, B., A. Will, and A. Hense, 2008: The Regional Climate Model COSMO-CLM (CCLM). *Meteor. Z.,* **17,** 347–348, doi:10.1127/0941-2948/2008/0309.

Rooney, G., and F. Bornemann, 2013: The performance of FLake in the Met Office Unified Model. *Tellus,* **1A,** 21363, doi:10.3402/tellusa.v65i0.21363.

Rossow, W. B., and R. A. Schiffer, 1999: Advances in understanding clouds from ISCCP. *Bull. Amer. Meteor. Soc.,* **80,** 2261–2287, doi:10.1175/1520-0477(1999)080<2261:AIUCFI>2.0.CO;2.

Rudolf, B., A. Becker, and U. Schneider, 2011: New GPCC full data reanalysis version 5 provides high-quality gridded monthly precipitation data. *GEWEX News,* Vol. 21, No. 2, International GEWEX Project Office, Silver Spring, MD, 4–5.

Saeed, F., A. Haensler, T. Weber, S. Hagemann, and D. Jacob, 2013: Representation of extreme precipitation events leading to opposite climate change signals over the Congo basin. *Atmosphere,* **4,** 254–271, doi:10.3390/atmos4030254.

Samuelsson, P., E. Kourzeneva, and D. Mironov, 2010: The impact of lakes on the European climate as simulated by a regional climate model. *Boreal Environ. Res.,* **15,** 113–129.

Savijärvi, H., 1997: Diurnal winds around Lake Tanganyika. *Quart. J. Roy. Meteor. Soc.,* **123,** 901–918, doi:10.1002/qj.49712354006.

——, and S. Järvenoja, 2000: Aspects of the fine-scale climatology over Lake Tanganyika as resolved by a mesoscale model. *Meteor. Atmos. Phys.,* **73,** 77–88, doi:10.1007/s007030050066.

Schmid, M., and A. Wüest, 2012: Stratification, mixing and transport processes in Lake Kivu. *Lake Kivu: Limnology and Biogeochemistry of a Tropical Great Lake,* J.-P. Descy, F. Darchambeau, and M. Schmid, Eds., Springer, 13–29, doi:10.1007/978-94-007-4243-7.

Schneider, U., A. Becker, P. Finger, A. Meyer-Christoffer, M. Ziese, and B. Rudolf, 2014: GPCC's new land surface precipitation climatology based on quality-controlled in situ data and its role in quantifying the global water cycle. *Theor. Appl. Climatol.,* **115,** 15–40, doi:10.1007/s00704-013-0860-x.

Sellers, P., and Coauthors, 1997: Modeling the exchanges of energy, water, and carbon between continents and the atmosphere. *Science,* **275,** 502–509, doi:10.1126/science.275.5299.502.

Semazzi, F. H. M., 2011: Enhancing safety of navigation and efficient exploitation of natural resources over Lake Victoria and its basin by strengthening meteorological services on the lake. North Carolina State University Climate Modeling Laboratory Tech. Rep., 104 pp. [Available online at http://climlab02.meas.ncsu.edu/HYVIC/Final_Report_LVBC.pdf.]

Song, Y., F. H. M. Semazzi, L. Xie, and L. J. Ogallo, 2004: A coupled regional climate model for the Lake Victoria basin of East Africa. *Int. J. Climatol.,* **24,** 57–75, doi:10.1002/joc.983.

Stackhouse, P. W., S. K. Gupta, S. J. Cox, T. Zhang, J. C. Mikovitz, and L. M. Hinkelman, 2011: 24.5-year surface radiation budget data set released. *GEWEX News,* Vol. 21, No. 1, International GEWEX Project Office, Silver Spring, MD, 10–12.

Stepanenko, V., S. Goyette, A. Martynov, M. Perroud, X. Fang, and D. Mironov, 2010: First steps of a Lake Model Intercomparison Project: LakeMIP. *Boreal Environ. Res.,* **15,** 191–202.

——, and Coauthors, 2013: A one-dimensional model intercomparison study of thermal regime of a shallow, turbid midlatitude lake. *Geosci. Model Dev.,* **6,** 1337–1352, doi:10.5194/gmd-6-1337-2013.

——, K. Jöhnk, and E. Machulskaya, 2014: Simulation of surface energy fluxes and stratification of a small boreal lake by a set of one-dimensional models. *Tellus,* **66A,** 21389, doi:10.3402/tellusa.v66.21389.

Stöckli, R., and Coauthors, 2008: Use of FLUXNET in the Community Land Model development. *J. Geophys. Res.,* **113,** G01025, doi:10.1029/2007JG000562.

Subin, Z. M., L. N. Murphy, F. Li, C. Bonfils, and W. J. Riley, 2012: Boreal lakes moderate seasonal and diurnal temperature variation and perturb atmospheric circulation: Analyses in the Community Earth System Model 1 (CESM1). *Tellus,* **64A,** 15639, doi:10.3402/tellusa.v64i0.15639.

Sun, L., F. Semazzi, F. Giorgi, and L. Ogallo, 1999: Application of the NCAR regional climate model to eastern Africa: 1. Simulation of the short rains of 1988. *J. Geophys. Res.,* **104,** 6529–6548, doi:10.1029/1998JD200051.

Sun, X., L. Xie, F. H. M. Semazzi, and B. Liu, 2014a: Effect of lake surface temperature on the spatial distribution and intensity of the precipitation over the Lake Victoria basin. *Mon. Wea. Rev.,* **143,** 1179–1192, doi:10.1175/MWR-D-14-00049.1.

——, ——, ——, and ——, 2014b: A numerical investigation of the precipitation over Lake Victoria basin using a coupled atmosphere-lake limited-area model. *Adv. Meteorol.,* **2014,** 960924, doi:10.1155/2014/960924.

Sylla, M. B., F. Giorgi, E. Coppola, and L. Mariotti, 2013: Uncertainties in daily rainfall over Africa: assessment of gridded observation products and evaluation of a regional climate model simulation. *Int. J. Climatol.,* **33,** 1805–1817, doi:10.1002/joc.3551.

Thiery, W., A. Martynov, F. Darchambeau, J.-P. Descy, P.-D. Plisnier, L. Sushama, and N. P. M. van Lipzig, 2014a: Understanding the performance of the FLake model over two African Great Lakes. *Geosci. Model Dev.,* **7,** 317–337, doi:10.5194/gmd-7-317-2014.

——, and Coauthors, 2014b: LakeMIP Kivu: Evaluating the representation of a large, deep tropical lake by a set of one-dimensional lake models. *Tellus,* **66A,** 21390, doi:10.3402/tellusa.v66.21390.

Tiedtke, M., 1989: A comprehensive mass flux scheme for cumulus parameterization in large-scale models. *Mon. Wea. Rev.,* **117,** 1779–1800, doi:10.1175/1520-0493(1989)117<1779:ACMFSF>2.0.CO;2.

Vanden Broucke, S., S. Luyssaert, E. Davin, I. Janssens, and N. P. M. van Lipzig, 2015: Temperature decomposition of paired site observations reveals new insights in climate models' capability to simulate the impact of LUC. *J. Geophys. Res.,* in press.

Verburg, P., and J. P. Antenucci, 2010: Persistent unstable atmospheric boundary layer enhances sensible and latent heat loss in a tropical great lake: Lake Tanganyika. *J. Geophys. Res.,* **115,** 5347, doi:10.1029/2009JD012839.

——, ——, and R. E. Hecky, 2011: Differential cooling drives large-scale convective circulation in Lake Tanganyika. *Limnol. Oceanogr.,* **56,** 910–926, doi:10.4319/lo.2011.56.3.0910.

Vizy, E. K., and K. H. Cook, 2012: Mid-twenty-first-century changes in extreme events over northern and Tropical Africa. *J. Climate,* **25,** 5748–5767, doi:10.1175/JCLI-D-11-00693.1.

Williams, K., J. Chamberlain, C. Buontempo, and C. Bain, 2015: Regional climate model performance in the Lake Victoria basin. *Climate Dyn.,* **44,** 1699–1713, doi:10.1007/s00382-014-2201-x.